

University of Minnesota  
ST. ANTHONY FALLS HYDRAULIC LABORATORY

Project Report No. 108

A STUDY OF FLOW OVER VENTILATED  
DISCONTINUITIES IN A BOUNDARY LAYER

by  
B. D. Ward,  
A. C. Young,  
and  
A. G. Anderson

Prepared for  
NATIONAL SCIENCE FOUNDATION  
Washington, D. C.  
NSF GK-722

June 1969  
Minneapolis, Minnesota

CONTENTS

Abstract. . . . . iii

List of Symbols . . . . . iv

Preface . . . . . vi

I. INTRODUCTION. . . . . 1

II. DESCRIPTION OF EXPERIMENTS. . . . . 2

    A. General Considerations. . . . . 2

    B. Test Procedures . . . . . 3

    C. Drag Measurements . . . . . 4

III. DISCUSSION AND RESULTS. . . . . 4

    A. Cavity Characteristics. . . . . 4

    B. Drag Reduction. . . . . 8

IV. CONCLUSIONS . . . . . 10

V. RECOMMENDATIONS FOR FURTHER STUDY . . . . . 11

List of References. . . . . 13

List of Figures (for 25 accompanying Figures)

Appendix -- ANALYSIS

    List of Symbols - Appendix. . . . . A-ii

    A. Linearized Theory . . . . . A-1

    B. Break-in-Grade. . . . . A-2

    C. Step. . . . . A-6

    D. Slot. . . . . A-7

    List of References - Appendix . . . . . A-10

    List of Figures - Appendix (for 3 accompanying Figures)

## ABSTRACT

At present hydrodynamicists are critically interested in ventilation as a means of vessel guidance and control. The injection of air into the boundary layer can also produce significant drag reduction benefits and cushion an abruptly changing flow boundary against the severity of cavitation damage in high velocity flows.

This report describes an experimental investigation of the characteristics of ventilated cavities situated in a boundary layer and their effects, including drag reduction. Study cases include free surface flows over ventilated boundary discontinuities in the form of a step, a slot, and a break-in-grade.

The observed cavities are generally similar to those found in the wake of supercavitating hydrofoils. The quantitative results refer to cavity length, air supply coefficient, and ventilation parameter. The maximum drag reduction obtained with a ventilated slot in a boundary layer over the smooth surface in the fully wetted case was on the order of fifteen per cent. The average flow velocity for the drag reduction experiment was from ten to nineteen feet per second. Empirical cavity results are also compared with irrotational linearized potential flow theory in the appendix. Only the step experiment showed good agreement with theory.

## LIST OF SYMBOLS

A, A'	Coefficients
A <sub>T</sub> , A <sub>L</sub>	Area of air introduction suit and of test plate
b	Test channel width
C	Length of boundary discontinuity
C <sub>w</sub>	Air supply coefficients $\frac{w}{\rho_a g T U} = \frac{U_a}{U}$
$\Delta C_D$	Drag reduction coefficient $\frac{\Delta D}{(\rho U^2 / 2) A_L}$
D	Drag force
F <sub>T</sub> , F <sub>d</sub>	Froude number, $\frac{U}{\sqrt{gT}}$ , $\frac{U}{\sqrt{gd}}$
K	Ventilation parameter, $\frac{P_r - P_c}{\rho U^2 / 2}$
K <sub>*</sub>	Critical ventilation parameter
L	'Floating' test plate length
l	Cavity length
m, n	Exponents
N	Power ratio
P <sub>D</sub>	Power gained by drag reduction
P <sub>r</sub>	Mainstream reference pressure
P <sub>c</sub>	Cavity pressure
P <sub>w</sub>	Power expended to ventilate
Q	Mainstream discharge
T	Characteristic height of discontinuities

U	Mainstream average velocity
$U_a$	Effective air velocity, $\frac{w}{\rho_a g T b}$
w	Weight rate of air flow
$\gamma$	Characteristic discontinuity angle
$\mu, \mu_a$	Mainstream and air dynamic viscosity
$\rho, \rho_a$	Mainstream and air mass density
$\sigma$	Surface tension (air-water interface)

## PREFACE

This report presents the results of an experimental investigation into the possible benefits of ventilation into the boundary layer of fluid flow by boundary discontinuities. Cavity characteristics and drag reduction were studied.

The research program was largely supported by Grant No. GK-722 from the National Science Foundation, and the text represents a final project report.

The help of Messrs. N. Pundarikanthan and J. Sieberlich in performing the experiments is acknowledged. Dr. K. Yalamanchili is responsible for the appendix, which deals with a linearized potential theory analysis of the boundary discontinuities studied experimentally.

# A STUDY OF FLOW OVER VENTILATED DISCONTINUITIES IN A BOUNDARY LAYER

## I. INTRODUCTION

The injection of a noncondensable gas into a liquid boundary layer has recently been considered theoretically [1]\* and experimentally [2,3] as a means of reducing skin friction drag on submerged surfaces. All of these studies recognized the drag-reducing potential of a two-phase system consisting of a thin film of air next to the boundary in a liquid boundary layer. A general introduction to single-phase injection into the boundary layer is given in the text by Schlichting [4].

Air must be injected as a continuous film along the solid boundary to effect significant drag reduction. Ventilation in the form of suspended gas bubbles does little to reduce skin friction drag. Pipe flow and open channel studies [5,6] have in fact shown that suspended air concentrations can significantly increase bulk velocity and the effective viscosity.

The benefits derived by injecting air into flow localities of possible cavitation damage have been postulated, but few quantitative studies as to the effectiveness of this form of imposed protection are available [7,8,9]. The larger ventilated air bubbles are thought to cushion the solid hydraulic surface against the high compressive pressures of cavitation bubble collapse. Injected air can be utilized, for example, to protect offsets in hydraulic structures and construction finish irregularities such as joints.

Another useful application of the two-phase boundary layer is in the guidance and control of underwater projectiles by air ventilation. Research sponsored by the Navy [10,11] found that torpedo control function forces created by selective ventilation compared favorably with those of existing underwater torpedoes. The control and stabilization of hydrofoils and underwater bodies by aeration is another topic of current interest and research. Tests performed for the Navy at the St. Anthony Falls Hydraulic Laboratory [12,13] have determined the air requirements and cavity characteristics for a ventilated, submerged hydrofoil.

---

\*Numbers in brackets refer to the List of References on page 13.

Taking full advantage of the hydrodynamic benefits obtainable from air ventilation into a boundary layer requires fundamental knowledge of cavity characteristics and the similarity of dynamic scaling effects. This report examines the nature of ventilated cavities by relating experimental cavity lengths and consequent air-flow rates to a characteristic ventilation parameter, boundary geometry, and resulting drag reduction. Cavity conditions were also analyzed according to linearized potential theory for finite depth of flow over the three test discontinuities experimentally studied (the slot, the step, and the break-in-grade) as an initial theoretical approximation, and this information is included in the appendix.

## II. DESCRIPTION OF EXPERIMENTS

### A. General Considerations

Horizontal free-surface-flow tests over isolated air-ventilated slot, step, and break-in-grade elements were performed in a transparent lucite channel test section 18 in. wide by 64 in. long (Figs. 1, 2, and 3). Analysis of the step and break-in-grade configurations was limited to cavity flow characteristics, with most attention being given to the slot case, where drag reduction due to ventilation was also studied.

Discharges of river water varying from 10 to 25 cfs were measured with an accuracy of  $\pm 1$  per cent by two calibrated Pitot cylinders mounted in the supply lines. Air for ventilation was obtained from the Laboratory's high-pressure air supply and was regulated by a pressure reducer and monitored by a series of orifices with associated differential manometers. Ventilation air for all test cavities was injected through a continuous row of 1/8-in. diameter holes leading to a 1/16-in. slot opening for uniform air distribution across the channel width.

A removable test channel bottom allowed for ease in installation of the slot, step, and break-in-grade boundary discontinuities. These elements were placed in the channel floor, as illustrated schematically in Fig. 2. The pressures upstream and downstream of the boundary discontinuities were recorded by piezometer taps selectively spaced along the centerline of the test channel bottom. The static pressure of the undisturbed flow was recorded at a side-wall tap four inches from the channel floor, while cavity reference pressure

was determined from two centerline taps located 1/2 in. and 1 in. downstream from the abrupt variation in test bottom boundary geometry.

A 0.06 in. flat-nosed Pitot tube was used to measure longitudinal, transverse, and vertical velocity profiles. Typical centerline and transverse velocity profiles taken just upstream of a discontinuity are shown in Fig. 4. For all flows tested, longitudinal velocity profiles indicated fully developed flow for inlet lengths of over sixty channel depths, although secondary flow effects were somewhat in evidence (Fig. 4c). A point gage was utilized to record the form of the free surface throughout the test section for all flows. The variation of pressure along the boundary discontinuity and the associated water surface profiles are given in Fig. 5 for a typical test flow over the step configuration, comparing fully wetted and ventilated conditions.

#### B. Test Procedures

Prior to each set of runs the water discharge was established and velocity profiles taken to assess flow development and aid in detection of any abnormal flow irregularities. Variables recorded during each run included cavity and upstream reference pressure, surface profile and piezometric head along the test section centerline, air and free-stream temperature, air supply, and cavity length. The slot boundary configuration was mounted in a null-balance floating plate bottom section, allowing the measurement of drag for this one geometry.

The fully wetted flow condition was tested before the injection of air into all three boundary discontinuities. The length of the ventilated cavity was determined through reference to a length scale etched on the channel bottom. Illumination of the cavity by a floodlight directed through the transparent test section allowed distinction of the somewhat irregular outline of the cavity shown in Figs. 6 and 7. For lower air flow rates where a reentrant jet was evidenced (details of cavity formation are given in the Discussion and Results section), the cavity length was defined as the distance from the plane of air injection to the visual origin of the reentrant jet. All pressure readings were simultaneously displayed on a piezometer tube panel.

### C. Drag Measurements

A floating test section allowing shear measurement was employed to determine incremental drag reduction due to ventilation into the contained slot element (Fig. 8). The test plate was mounted on flexure members which permitted free movement in the direction of flow. The floating plate acted as a null-reading device as displacement from zero deflection was determined by a linear differential transformer sensitive to  $10^{-4}$  in. The plate was connected via a small pulley to a direct reading spring vernier scale which permitted balancing of the drag force by applying a known external force. The shear measuring device was calibrated, in place, under a static head of water before each series of runs, and dead weights were utilized for the fundamental calibration of the restoring spring constant.

The floating element bottom was enclosed by a gap of approximately 0.08 inches. Injected dyes in test flows indicated almost no downstream flow through the test plate, although secondary flows were observed in a weak lateral circulation through the floating plate. The effects of the lateral flow were thought to be considerably less than the standard error from the recorded mean of force measured.

## IV. DISCUSSION AND RESULTS

### A. Cavity Characteristics

The concept of controlling and altering flow behavior near a boundary by injecting air requires insight into the behavior of the resulting air layer. The cavity characteristics of the slot, step, and break-in-grade can be considered dependent on a long list of geometrical and fluid flow variables given by

$$l = f_1(U_a, \rho_a, T, P_r, P_c, U, \rho, \mu, g, \gamma, d, \sigma) \quad (1)$$

where  $l$ , the cavity length, is contained within the test discontinuities and

$U, U_a$  = free stream mean velocity and ventilated air mean velocity, respectively;

$\rho, \rho_a$  = mass density of the mainstream and of ventilated air;

$\mu, \mu_a$  = dynamic viscosity of the free stream and of injected air;

$T$  = characteristic height of the boundary discontinuity;

$P_r$  = free stream reference pressure;

$P_c$  = cavity pressure;

$g$  = gravitational constant;

$\gamma$  = characteristic discontinuity angle;

$d$  = reference free-surface depth just upstream of the cavity; and

$\sigma$  = surface energy (ventilating gas-free stream interface).

The relationship between the cavity length and the variables cited can be arranged non-dimensionally in the form

$$\frac{l}{T} = f_2 \left( \frac{d}{T}, C_w, K, \frac{U^2}{gT}, \frac{Ud}{v}, \gamma, \frac{\rho_a}{\rho}, \frac{\mu_a}{\mu}, \frac{TU^2}{\sigma} \right) \quad (2)$$

where  $C_w$  = air supply coefficient and  $K$  = ventilation parameter. For test conditions in the experiments described the above expression was reduced to

$$\frac{l}{T} = f_3 \left( C_w, K, \frac{U^2}{gT} \right) \quad (3)$$

Since the ventilated gas and the free stream were air and water, respectively, the depth was always several orders of magnitude larger than  $T$ , and  $\gamma$  was held constant except for the break-in-grade tests. The pertinent flow surface, then, relating to gravity effects was the cavity-mainstream interface. Although the characteristic Weber and Reynolds numbers were considered negligible in arriving at Eq. (3), their effects can still be expected to affect experimental results somewhat.

Not all the variables given on the right-hand side of Eq. (3) are independent.  $C_w$ , a kinematic air supply flow coefficient, and  $K$  are intrinsically related to each other as affected by Froude number  $F_T = U/\sqrt{gT}$ , discontinuity geometry, and the combination of effects from the terms appearing in Eq. (2) and omitted in Eq. (3). The mainstream velocities tested were low enough ( $10 < U, \text{fps} < 25$ ) that Froude number effects varied significantly in influence

as velocity of discharge was varied (since depth was maintained constant, velocity varied directly with discharge). A comparison of  $C_w$  versus  $K$  for any one particular geometry was dependent on  $T$  and  $U$  in an unsystematic manner because of the varying sensitivity to  $F_T \sim Q/\sqrt{T}$  throughout any test series. This phenomenon is dramatically illustrated in Figs. 9a and 9b, where ventilation into 1/8-, 3/8-, and 3/4-inch steps demonstrated a decreasing dependence upon  $F_T$  with increasing mainstream velocity until  $C_w$  and  $K$  became direct dependent and insensitive to  $F_T$  at the highest Froude numbers ( $7.5 < F_T < 44$ ). Eventually as  $K$  decreased with increased air injection the ventilation parameter remained constant, and further addition of air did little to affect cavity behavior. Phenomenologically, the cavity which started and grew bounded by progressively weaker reentrant jets literally blew open, and the reentrant jets disappeared. Trailing "finger-like" vortices then served to entrain the air for eventual delivery to the boundary layer flow above. Beyond this "fully ventilated cavity" little further growth in cavity length or change in cavity pressure was witnessed with additional air ventilation. Figures 10a, 10b, and 11 indicate the above trends for flow by the ventilated slot and break-in-grade cases.

The reentrant jet cavity (the developing cavity condition) was seen to exist in two distinct forms. The cavity for low air discharges consisted of an air-water bubbly mixture whose oscillating motion was controlled by the discontinuity wake condition. As air injection was further increased the cavity became completely air-filled, but was still bounded by a weak reentrant jet pattern. Additional aeration eventually produced the final nonreentrant-fully ventilated cavity condition. Photographs depicting both the air-water mixture and the air-filled reentrant jet cavities are given in Figs. 6 and 7.

It must be noted that in the slot geometries tested the ventilation parameter was negative for extremely high air injection rates. This is not contradictory to accepted principles of cavity analysis, as the cavity pressure recording taps were at a lower piezometric datum than the upstream reference taps (see Fig. 5). At extremely high air injection rates the cavity static pressure eventually became greater than the reference pressure, producing a negative value of  $K$ . The fully vented cavity was seen to occur at values of  $K$  approaching zero, and this critical ventilation parameter was designated by  $K_*$ . The qualitative value of Fig. 11 describing  $C_w$  versus  $K$  for the break-in-grade case was somewhat obscured by the presence of the additional complexities

of large boundary angles and Froude effects difficult to assess. The data of Fig. 11, however, do indicate a definite empirical consistency between  $C_w$  and  $K$  for wide variations in the dependent variables listed in Eq. (3), but are not describable by a definite set of equations.

The experimentally determined cavity length can be discussed in terms of  $K$  or  $C_w$  interchangeably. Since the linearized theory was developed in terms of the ventilation parameter, Figs. 12, 13, and 14 illustrate for the step, slot, and break-in-grade the variation of cavity length with variation in the ventilation parameter,  $K$ . For design purposes cavity length could most easily be evaluated for variation of the air supply coefficient, and corresponding plots of  $l$  versus  $C_w$  for all configurations tested are also included in Figs. 15 through 17 to facilitate analysis. The desirability of a significant dimensionless ordinate,  $l/T$ , in Figs. 12 through 17 is precluded by the absence of geometric and dynamic scaling involving the characteristic magnitude of the boundary discontinuity.

The step case clearly demonstrates the two reentrant jet cavity regimes already outlined. In Fig. 12 the cavity length is seen to jump rather abruptly to a larger value as the cavity is in the process of changing from an air-water mixture to the air-filled condition. Comparing linearized irrotational theory with experimental results shows close agreement for  $l$  versus  $K$  for the step, as shown in Fig. 18, for the entire range of  $K$  even though irrotational flow results are completely insensitive to changes in the nature of the cavity. Figure 15, in which  $l$  is plotted versus  $C_w$  for the experimental step geometry, clearly illustrates the full range of Froude number effects on cavity characteristics. Cavity length becomes heavily dependent upon  $F_T$  at low Froude number (large  $T$  and small  $Q$ ), while high Froude numbers existing with the smallest step indicate little sensitivity to  $F_T$ . The jump in cavity length signifying an air-filled reentrant jet cavity is, as seen in Fig. 12, unmistakable.

The slot configuration given in Fig. 13 includes an envelope of  $K_*$ , indicating initiation of the fully ventilated cavity for the three geometries tested. Figure 19 points out the inadequacy of the linearized theory in predicting cavity length for the slot case. The slot configuration which contained the cavity within the finite slot boundaries was then less amenable to representation by theory than the unbounded step geometry.

Theoretical results given in Fig. 20 for the break-in-grade closely approximate the variation of  $l$  with  $K$  for only a limited range of test data. The cavity for the break-in-grade case is not contained within the boundary discontinuity, as shown in Figs. 14 and 17, and the functional relationships with  $K$  and  $C_w$  become strongly dependent upon free-stream velocity for this boundary form. The extreme curvature of the streamlines experienced experimentally in this same case also limits the usefulness of comparison with the mathematical model.

The feasibility of plotting a relationship in the form  $l$ , or  $l/T = A(C_w)^m$ , was considered for the geometries tested. Despite the exponent  $m$  possessing a value very close to  $3/5$  for all boundary discontinuities tested, the coefficient  $A$  could not be considered universal for even one type of discontinuity and was an irregular function of  $T$ ,  $\gamma$ , and  $U$ .

#### B. Drag Reduction

The slot was the only boundary discontinuity suitably equipped to measure directly the drag reduction due to ventilation in the boundary layer. Figure 21 indicates the two distinct zones of drag reduction corresponding to the reentrant and fully vented cavity regimes as specified by the maximum cavity length. The equation  $\Delta C_D = \Delta D / (\rho U^2 / 2) A_L$  is based on the difference between the fully wetted and the ventilated test plate. The actual overall drag reduction when compared to the flat plate case will be somewhat diminished by the form and pressure drag due to placement of the discontinuity on what was originally a smooth, continuous surface (see Fig. 22).

As shown in Fig. 23,  $\Delta C_D$  increases linearly in a dramatic fashion with an increasing air supply coefficient until the maximum cavity length is approached. As the cavity nears the fully vented condition, drag reduction falls off drastically and little further benefit is gained by increasing the air injection. As in the case of  $l$  versus  $C_w$ ,  $\Delta C_D$  versus  $C_w$  might be expressed, for the reentrant jet cavity, as a power law in the form  $\Delta C_D = A'(C_w)^n$ . From Fig. 23,  $n$  could be set equal to unity, but again, as for the cavity length, dynamic and geometric similitude is lacking, and  $A'$  cannot be evaluated as a simple function of  $T$  or  $F_T$ . The drag reduction parameter is shown to be linearly dependent on cavity length for a reentrant jet cavity with  $l$  less than its maximum value in Fig. 24. The line given by

$\Delta C_D = 0.0048 \ell/L$  only grossly represents the actual data, especially at smaller cavity lengths.

In considering the effectiveness of ventilating the boundary layer to promote drag reduction, the power ratio is defined as follows:

$$N = \frac{P_D}{P_W} = \frac{\text{Power gained by drag reduction}}{\text{Power expended for ventilation}} \quad (4)$$

where  $P = (\Delta D)U$  and  $P_W$  can be found by ignoring frictional resistance in the supply lines and making use of Bernoulli's equation giving

$$P_W = (P_c + \frac{\rho_a U_a^2}{2}) T_b U_a$$

with  $T_b$  representing the characteristic area of the ventilation cavity. By referring to the fundamental definitions for  $C_w$ ,  $K$ , and  $\Delta C_D$  given in the List of Symbols, Eq. (4) can be rewritten as

$$\left( \frac{A_L}{A_T} \right) \left( \frac{\Delta C_D}{C_w} \right) \left\{ \frac{1}{-K + \frac{2}{F_d^2} + \frac{\rho_a}{\rho} C_w^2} \right\} \quad (5)$$

where  $A_L$  and  $A_T$  are characteristic areas of the test plate and slot, respectively;  $F_d$  is the Froude number referenced to channel depth; and  $K$  is dependent upon  $C_w$ .

For the experiments performed,  $(\rho_a/\rho)C_w^2$  is extremely small compared to the  $K$  and  $2/F_d^2$  terms, while  $A_L/A_T$  is a constant for all slot configurations. The mainstream velocity and the ventilation parameter are, then, the critical variables controlling drag reduction in these tests, as the depth of flow for the slot case did not vary. Due to the unspecified interdependency of the variables represented in Eq. (5), determination of maximum power ratio by differentiation with a suitable independent variable is impossible.

Figure 25 plots  $N$ , the power ratio, against  $K$  with varying values of discharge over the largest slot for illustration. The maximum value of  $N$  was rapidly approached after the onset of air injection and was attained well within the reentrant jet cavity range. Thereafter  $N$  decreased slowly, then

increased slightly, and finally dropped precipitously with all further increases in ventilation as it approached  $K_*$  and beyond. The maximum power ratio attained in this slot test was slightly greater than eight.

#### IV. CONCLUSIONS

Of the configurations tested, the step configuration allowed for the optimum distribution of ventilating air, although some variation of the slot form would probably be more practical for application to ships and other wetted flow surfaces. The break-in-grade configuration proved least desirable for ventilation, as the air film could not follow the negatively sloping boundary closely, which meant that effective drag reduction was unlikely. These results were anticipated, and the break-in-grade was tested chiefly because it closely approximates many hydraulic irregularities where ventilation could be utilized to reduce cavitation damage. In general for maximum performance the ventilating gas should be introduced into a stream of high relative velocity to delay diffusion of gas away from the wall and into the boundary layer. The eventual onset of natural cavitation at velocities higher than witnessed in these tests will significantly affect gas injection requirements, but may provide further justification for the use of ventilation to alter and control the flow near a submerged wall.

The distinct reentrant jet and fully ventilated cavity regimes observed closely paralleled previous hydrofoil experiments cited. In all practical cases, especially that of a series arrangement of discontinuities, the cavity should be maintained well within the reentrant jet regime for greatest operating efficiency. Little additional change in cavity performance occurs with increased ventilation after the fully ventilated case is attained.

The Froude number controls to a great extent the optimum sizing of characteristic boundary discontinuity heights. The smallest slot and step geometries tested do, for a given air discharge, produce a cavity covering more surface area while minimizing the detrimental effects of additional form drag. The interaction between discontinuities spaced in tandem would also set restrictive criteria for selection of suitable geometry.

The measurements of drag for ventilation into the slot configurations indicated the benefits of drag reduction due to ventilation. Drag reduction

was approximately proportional to cavity length and was therefore unaffected by further addition of gas after full ventilation. Much more energy is required to maintain ventilation than is recovered due to drag reduction. The maximum power ratio for ventilation occurs early during the gas injection process. Efficiency is secondary, however, to the exciting possibility of extending the present maximum obtainable speed of submerged bodies by reducing drag and cavitation effects. Although for the studies reported on here the maximum reduction in drag over the smooth surface in the fully wetted case was on the order of 15 per cent, increasing free stream velocity should raise this value considerably for probable prototype conditions.

The experiments performed and discussed in this report demonstrate clearly the improbability of obtaining complete dynamic and geometric scaling for ventilated discontinuities in a boundary layer. Even when analysis is restricted to the reentrant jet cavity condition, the number of variables and the complexity of their combined effects preclude routine systematic appraisal.

It is hoped that the experiments presented will stimulate further analysis, both theoretical and experimental, into the promising phenomenon of fluid boundary ventilation. To this end a list of recommendations for further study follows.

#### V. RECOMMENDATIONS FOR FURTHER STUDY

The results summarized in this report point toward some possible modifications of the present study. In addition, several completely new investigations which might prove useful in advancing the understanding of the ventilation phenomenon are described below.

1. A theoretical study extending consideration to gravity effects and rotational nonlinear distribution of vorticity could be undertaken.
2. Placement of a boundary discontinuity in a uniform free stream (i.e., a towing basin) would allow for experimental comparison of uniform flow and boundary layer conditions.
3. The possibility of ventilation via a series of similar boundary configurations should be examined. Emphasis in such tests could include analysis of suitable discontinuity geometry under the criteria of optimum cavity and drag reduction characteristics.

4. The cavity should be aligned in the direction of gravity by placing boundary discontinuities in the sidewall of a test section. (Positioning in the roof of a closed test section would utilize buoyant gravity effects even further to create optimal cavity conditions.)
5. Free stream velocities should be increased to 40 to 50 fps to obtain maximum drag reduction, reduce unsystematic Froude effects, and create the conditions necessary for natural cavitation. The effect of ventilation in buffering the surface against damage from collapsing cavitation bubbles could be evaluated for this case.

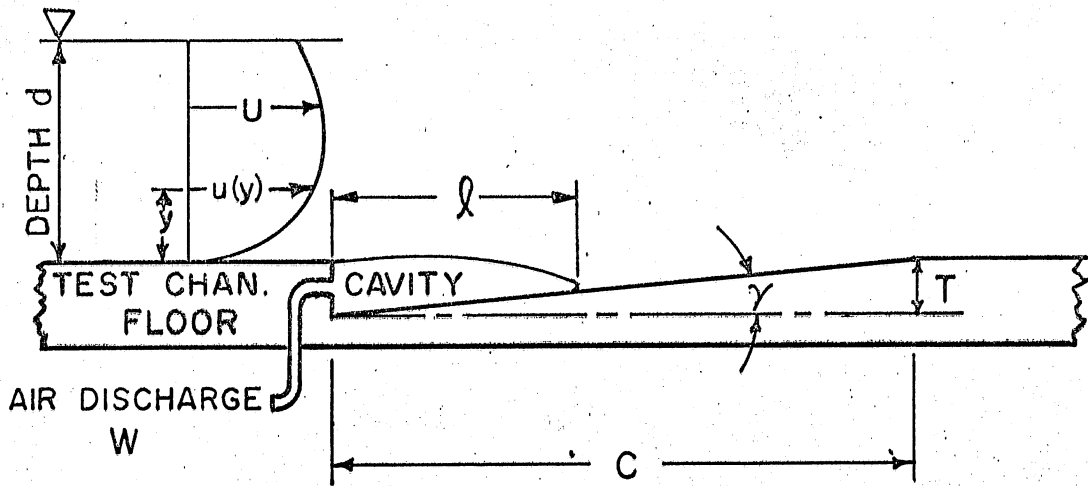
LIST OF REFERENCES

- [1] Sparrow, E. M.; Jonsson, V. K.; and Eckert, E. R. G., "A Two-Phase Boundary Layer and Its Drag-Reduction Characteristics," Transactions ASME, Journal of Applied Mechanics, June 1962, pp. 408-414.
- [2] Bradfield, W. S.; Barkdoll, R. D.; and Byrne, J. T., Film Boiling on Hydrodynamic Bodies, Research Note 37, Convair Scientific Research Laboratory, San Diego, December 1960.
- [3] Stefan, H. G. and Anderson, A. G., Cavity Formation and Associated Drag in a Supercavitating Flow over Wedges in a Boundary Layer, Project Report No. 69, St. Anthony Falls Hydraulic Laboratory, University of Minnesota, April 1964.
- [4] Schlichting, H., Boundary Layer Theory, McGraw-Hill Book Co., Inc., New York, 4th Edition, 1960, Chapter 13.
- [5] James, W. and Silberman, E., Two-Phase Flow Studies in Horizontal Pipes with Special Reference to Bubbly Mixtures, Technical Paper No. 26-B, St. Anthony Falls Hydraulic Laboratory, University of Minnesota, September 1958.
- [6] Straub, L. G. and Anderson, A. G., "Self-Aerated Flow in Open Channels," Transactions, ASCE, Vol. 125, 1960, pp. 456-486.
- [7] Thiruvengadam, A.; Preiser, H. S.; and Waring, S., Handbook of Cavitation Damage, Hydronautics, Inc., March 1965, pp. 151-153.
- [8] Mousson, J. M., "Pitting Resistance of Metals Under Cavitation Conditions," Transactions, ASME, Vol. 59, 1957, pp. 399-408.
- [9] Ball, J. W., "Construction Finishes and High-Velocity Flow," Journal of the Construction Div., ASCE, September 1963, pp. 91-110.
- [10] Lang, T. G.; Daybell, D. A.; and Smith, K. E., Water-Tunnel Tests of Hydrofoils with Forced Ventilation, NAVORD Report 7008, November 1959.
- [11] Ascosta, A. J. and Wade, R. B., Selectively Ventilated Ring Wing Hydrofoils, Report No. E-1382, Hydrodynamics Laboratory, CIT, August 1967.
- [12] Schiebe, F. R. and Wetzel, J. M., Ventilated Cavities on Submerged Three-Dimensional Hydrofoils, Technical Paper No. 36-B, St. Anthony Falls Hydraulic Laboratory, University of Minnesota, December 1961.
- [13] Schiebe, F. R. and Wetzel, J. M., Further Studies of Ventilated Cavities on Submerged Bodies, Project Report No. 72, St. Anthony Falls Hydraulic Laboratory, University of Minnesota, October 1964.

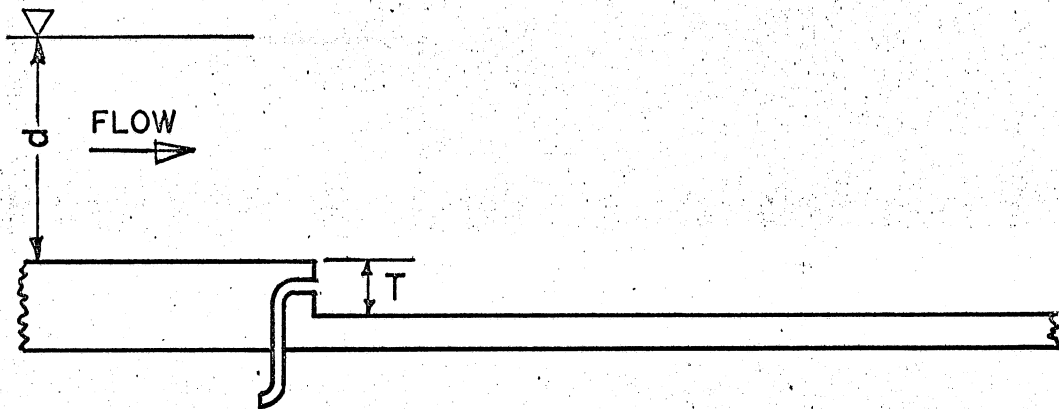
## LIST OF FIGURES

- FIGURE 1 Definition Sketch of Ventilated Boundary Discontinuities
- FIGURE 2 Test Section with Dynamometer and other measuring devices
- FIGURE 3 Test Elements: Break-in-Grade, Step, and Slot
- FIGURE 4a Centerline Velocity Profiles Immediately Upstream of Slot Discontinuity with Varying Discharge
- FIGURE 4b Transverse Velocity Profile Immediately Upstream of Slot Discontinuity
- FIGURE 4c Centerline Velocity Profiles Immediately Upstream of Break-in-Grade and Step Discontinuities
- FIGURE 5 Typical Water Surface and Pressure Profiles With and Without Ventilation
- FIGURE 6 Typical Air-Water Mixture Reentrant Jet Cavity. Step Height =  $3/4$  in., Velocity = 10.75 ft/sec, Air Discharge =  $5.2 \times 10^{-3}$  lbs/sec, Cavity Length = 7.5 in.
- FIGURE 7 Typical Air-Filled Reentrant Jet Cavity. Step Height =  $3/4$  in., Velocity = 10.75 ft/sec, Air Discharge =  $7.45 \times 10^{-3}$  lbs/sec, Cavity Length = 9.3 in.
- FIGURE 8 Floating Element Test Section with Slot Discontinuity, Spring-Steel Flexures, and Bellow Connection to Air Supply System
- FIGURE 9a Air Supply Coefficient versus Ventilation Parameter for a Step
- FIGURE 9b Air Supply Coefficient versus Ventilation Parameter for a Step
- FIGURE 10a Air Supply Coefficient versus Ventilation Parameter for the Slot
- FIGURE 10b Air Supply Coefficient versus Ventilation Parameter for the Slot
- FIGURE 11 Air Supply Coefficient versus Ventilation Parameter for the Break in Grade
- FIGURE 12 Length of Cavity versus Ventilation Parameter for the Step
- FIGURE 13 Length of Cavity versus Ventilation Parameter for the Slot
- FIGURE 14 Length of Cavity versus Ventilation Parameter for the Break in Grade
- FIGURE 15 Length of Cavity versus Air Supply Coefficient for the Step
- FIGURE 16 Length of Cavity versus Air Supply Coefficient for the Slot

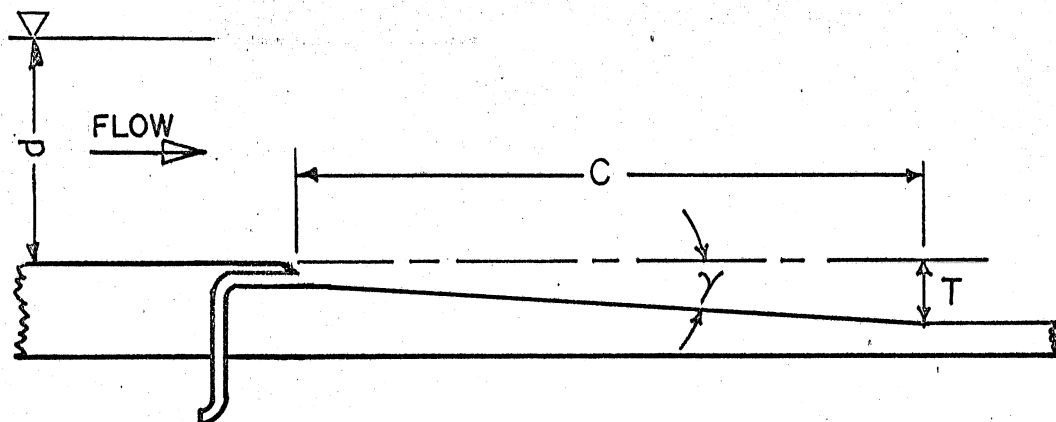
- FIGURE 17 Length of Cavity versus Air Supply Coefficient for the Break in Grade
- FIGURE 18 Comparison of Experimental Results with Linearized Theory for the Step
- FIGURE 19 Comparison of Experimental Results with Linearized Theory for the Slot
- FIGURE 20 Comparison of Experimental Results with Linearized Theory for the Break in Grade
- FIGURE 21 Differential Drag Parameter versus Ventilation Parameter for the Slot
- FIGURE 22 Drag Variation with Mean Velocity for the Smooth Plate and the Slot
- FIGURE 23 Differential Drag Parameter versus Air Supply Coefficient for the Slot
- FIGURE 24 Differential Drag Parameter versus Cavity Length Ratio for the Slot
- FIGURE 25 Power Ratio versus Ventilation Parameter for the Slot



(A) SLOT



(B) STEP



(C) BREAK-IN-GRADE

FIGURE 1. DEFINITION SKETCH OF VENTILATED BOUNDARY DISCONTINUITIES

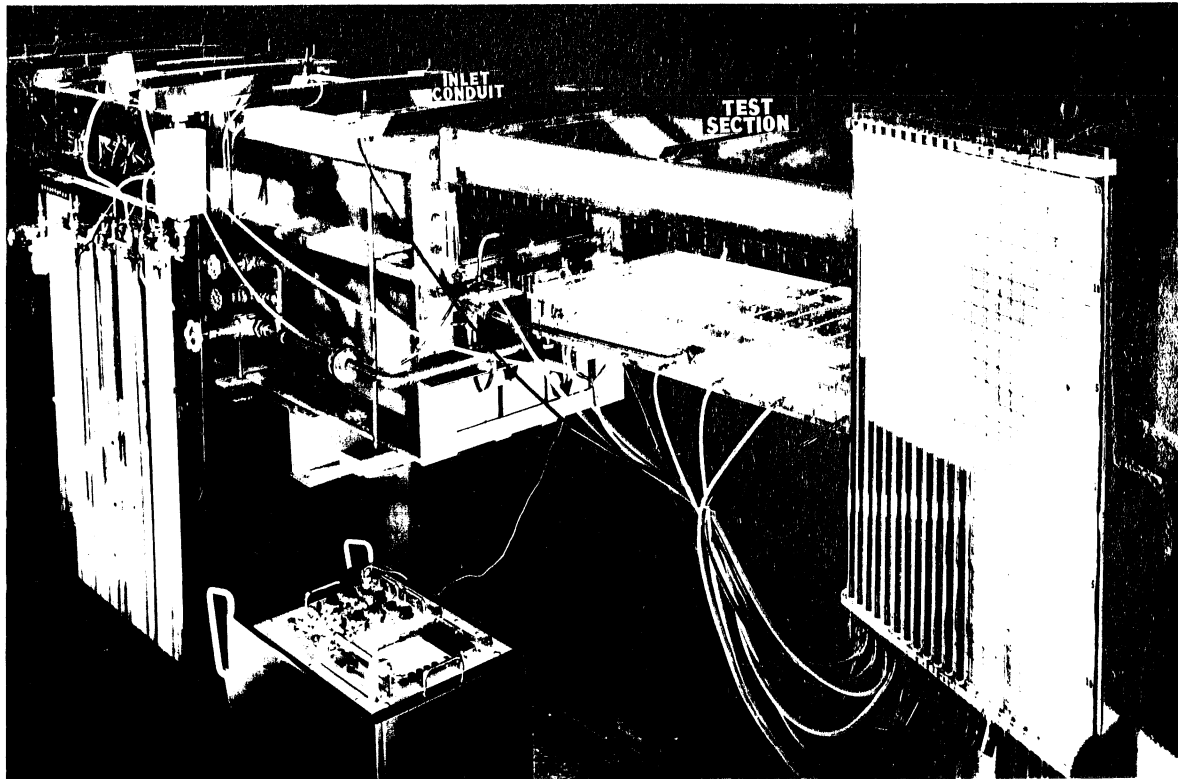


Fig. 2 - Test Section with Dynamometer and other measuring devices

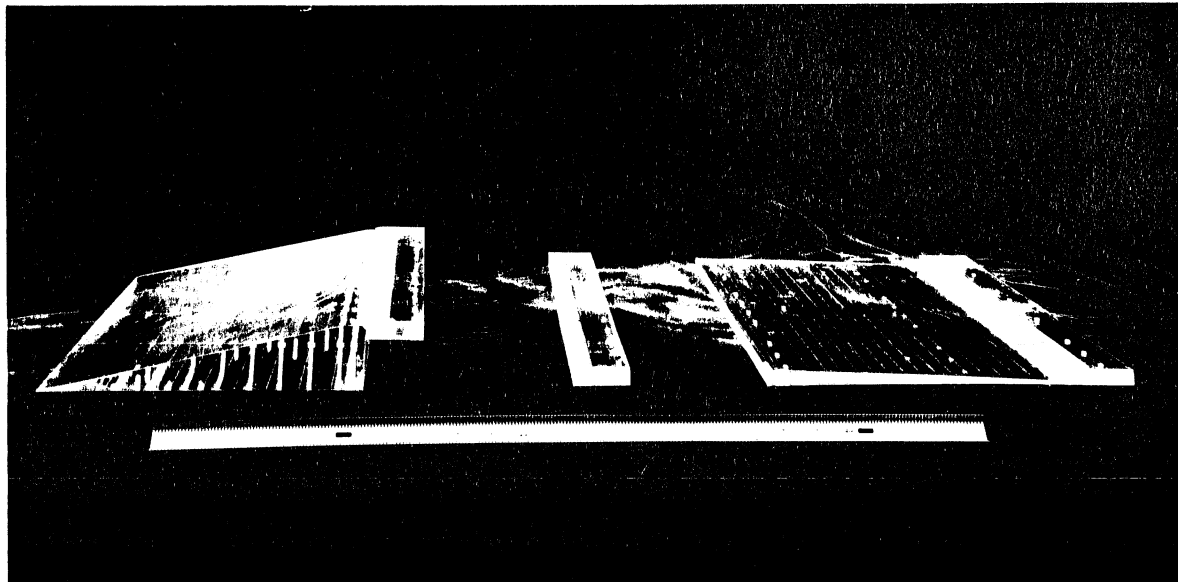


Fig. 3 - Test Elements: Break-in-Grade, Step, and Slot (from left to right)

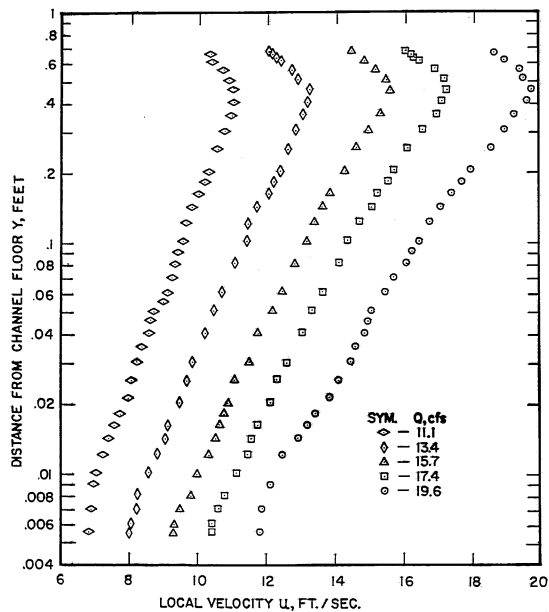


Fig. 4a - Centerline Velocity Profiles immediately upstream of Slot Discontinuity with Varying Discharge

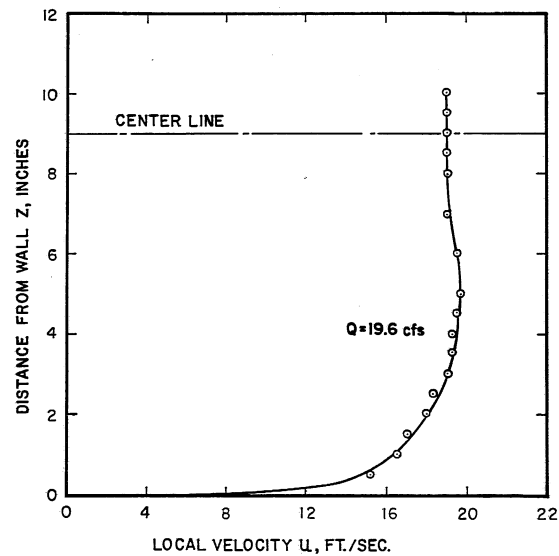


Fig. 4b - Transverse Velocity Profile immediately upstream of Slot Discontinuity

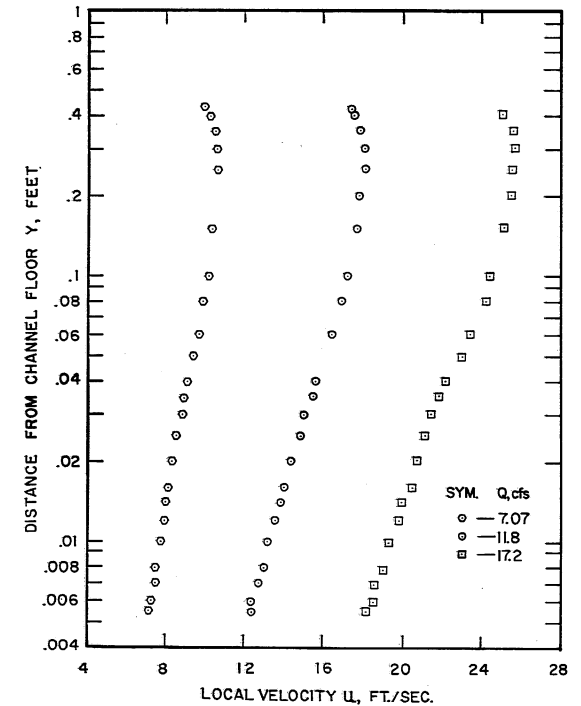


Fig. 4c - Centerline Velocity Profiles immediately upstream of Break-in-Grade and Step Discontinuities

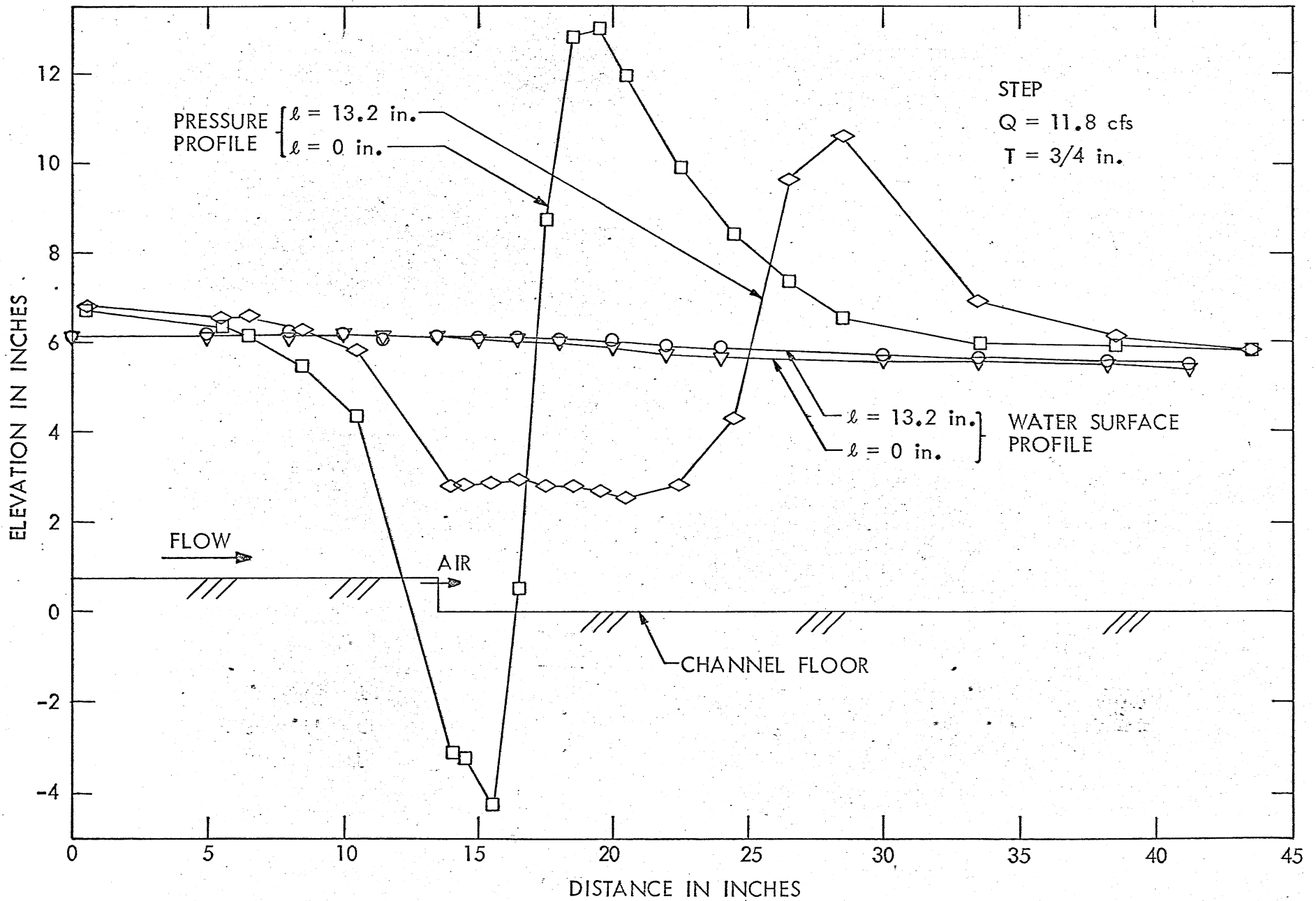


Fig. 5 - Typical Water Surface and Pressure Profiles With and Without Ventilation



a.



b.



c.

Fig. 6 - Typical Air-Water Mixture Reentrant Jet Cavity. Step Height = 3/4 in., Velocity = 10.75 ft/sec, Air Discharge =  $5.2 \times 10^{-3}$  lbs/sec, Cavity Length = 7.5 in.



a.



b.



c.

Fig. 7 - Typical Air-Filled Reentrant Jet Cavity. Step Height =  $3/4$  in.,  
Velocity = 10.75 ft/sec, Air Discharge =  $7.45 \times 10^{-3}$  lbs/sec,  
Cavity Length = 9.3 in.

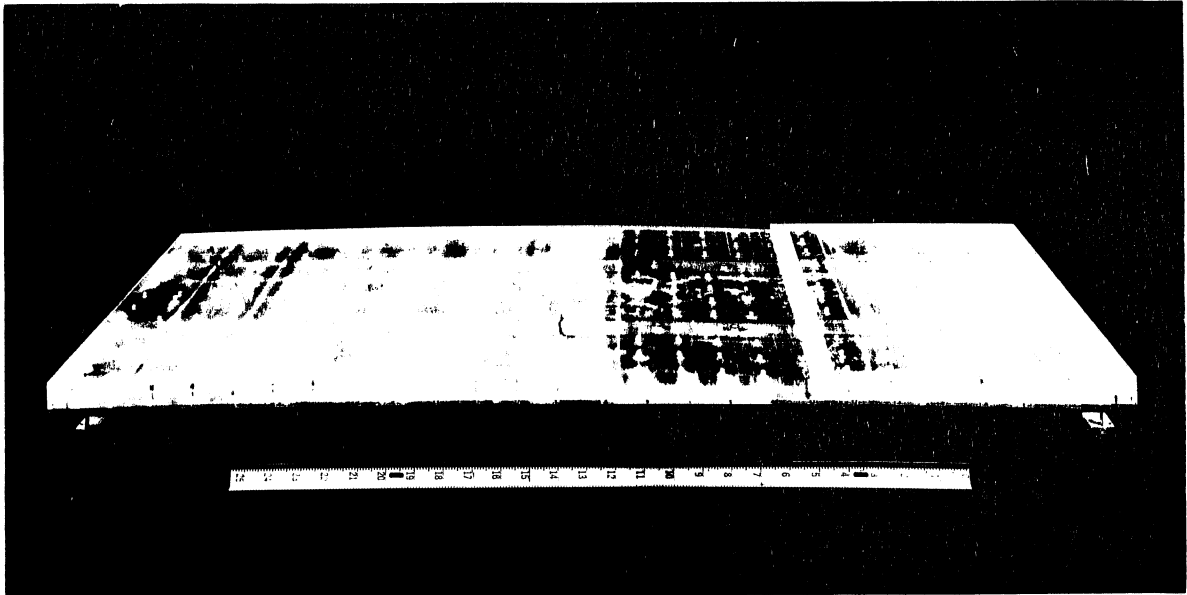


Fig. 8 - Floating Element Test Section with Slot Discontinuity, Spring-steel Flexures, and Bellow Connections to Air Supply System

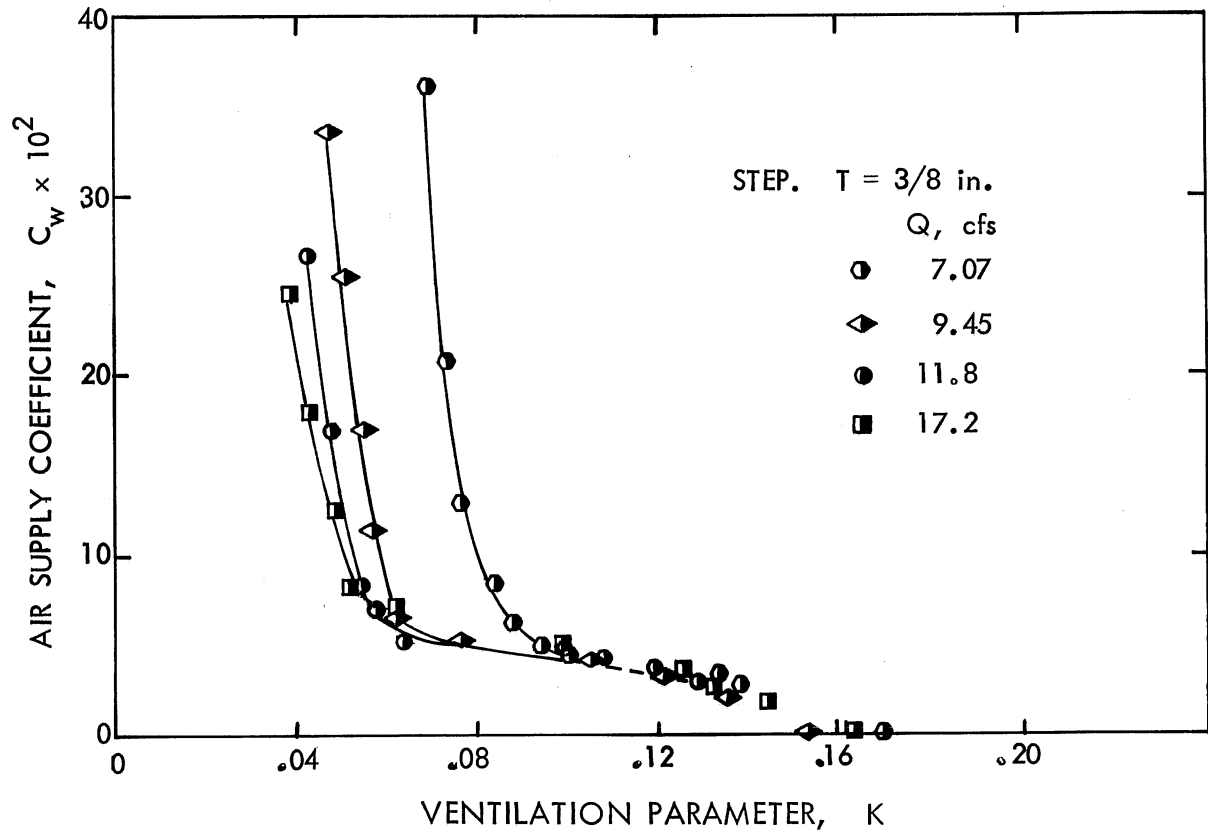


Fig. 9a - Air Supply Coefficient versus Ventilation Parameter for a Step

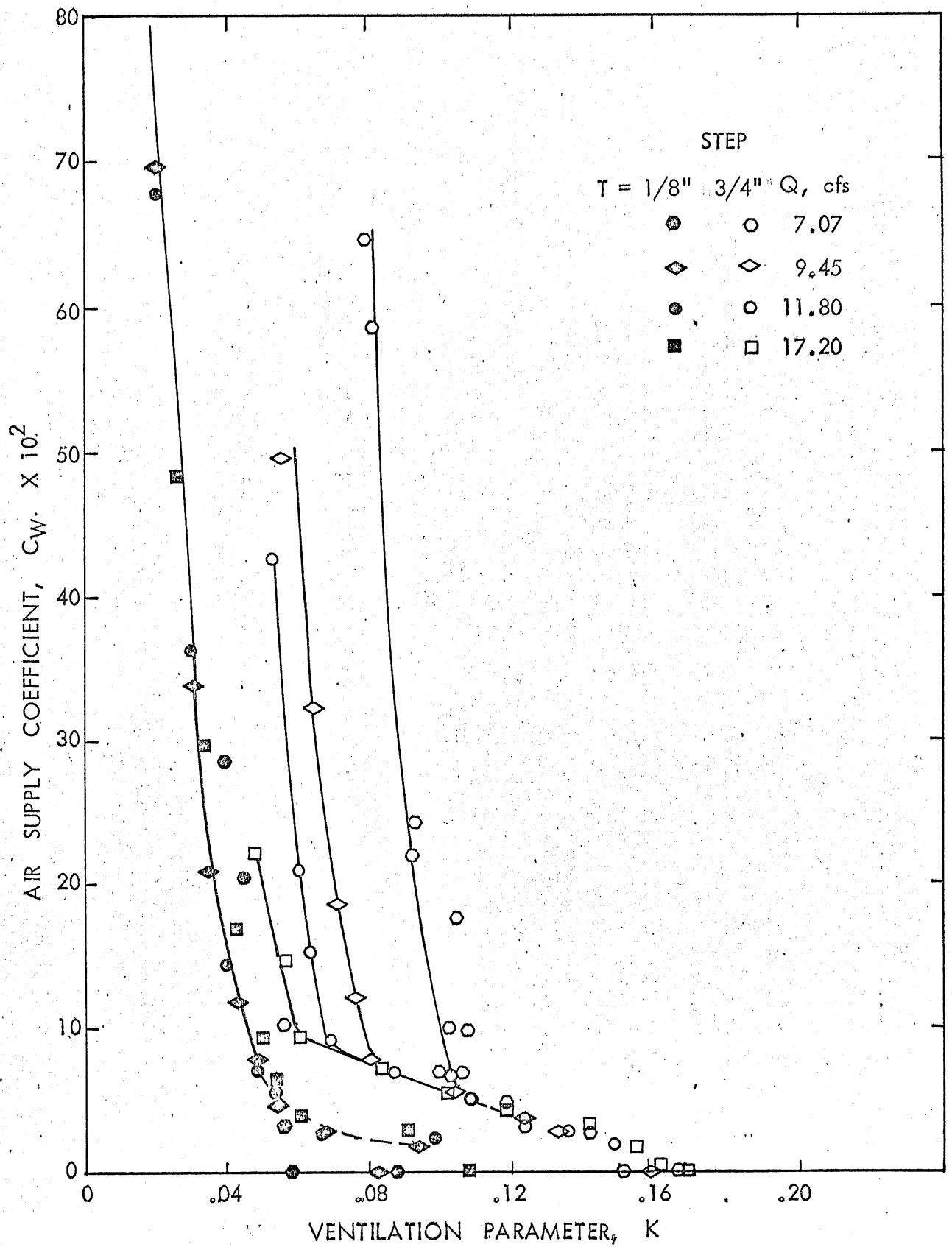


Fig. 9b - Air Supply Coefficient versus Ventilation Parameter for a Step

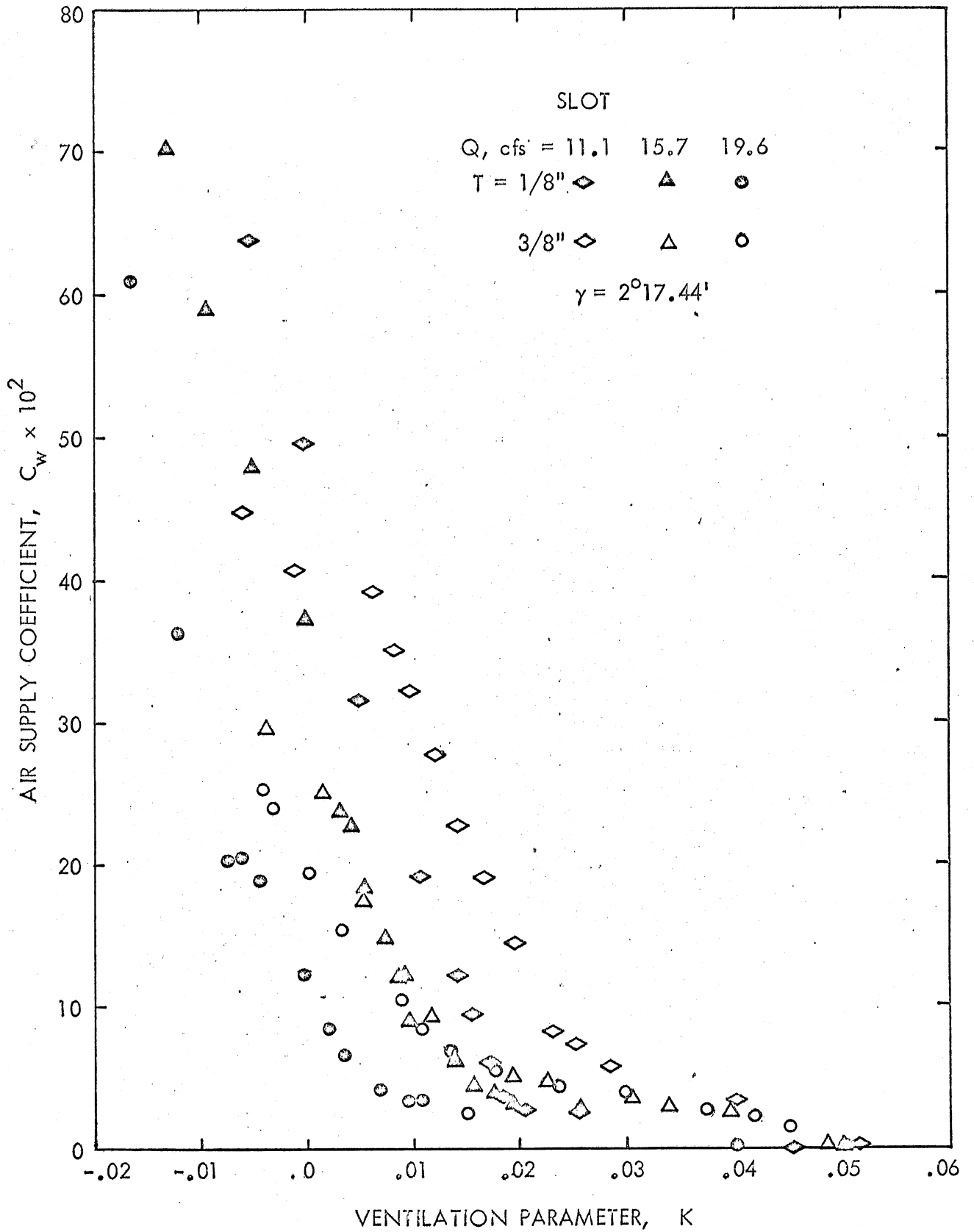


Fig. 10a - Air Supply Coefficient versus Ventilation Parameter for the Slot

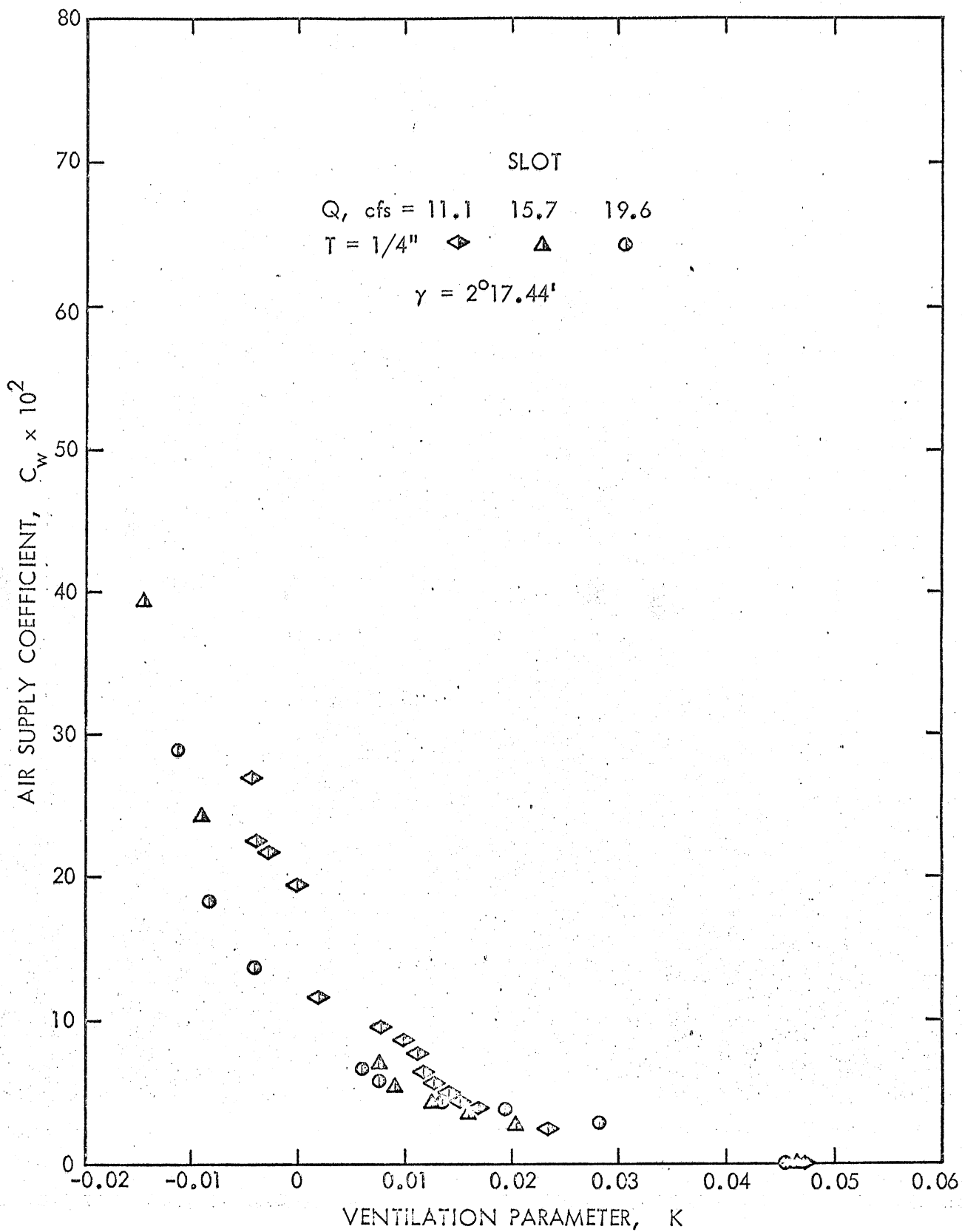


Fig. 10b - Air Supply Coefficient versus Ventilation Parameter for the Slot

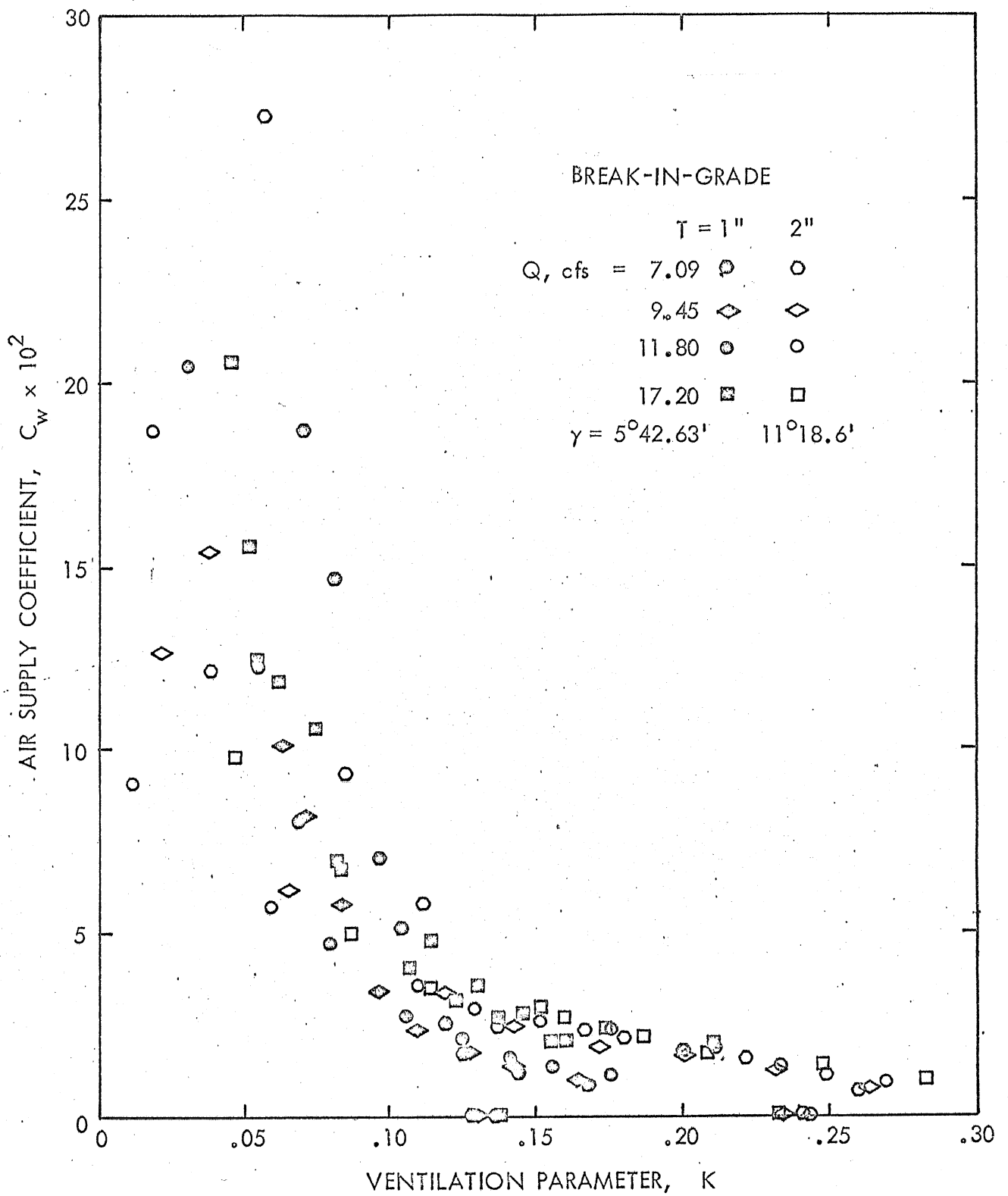


Fig. 11 - Air Supply Coefficient versus Ventilation Parameter for the Break-in-Grade

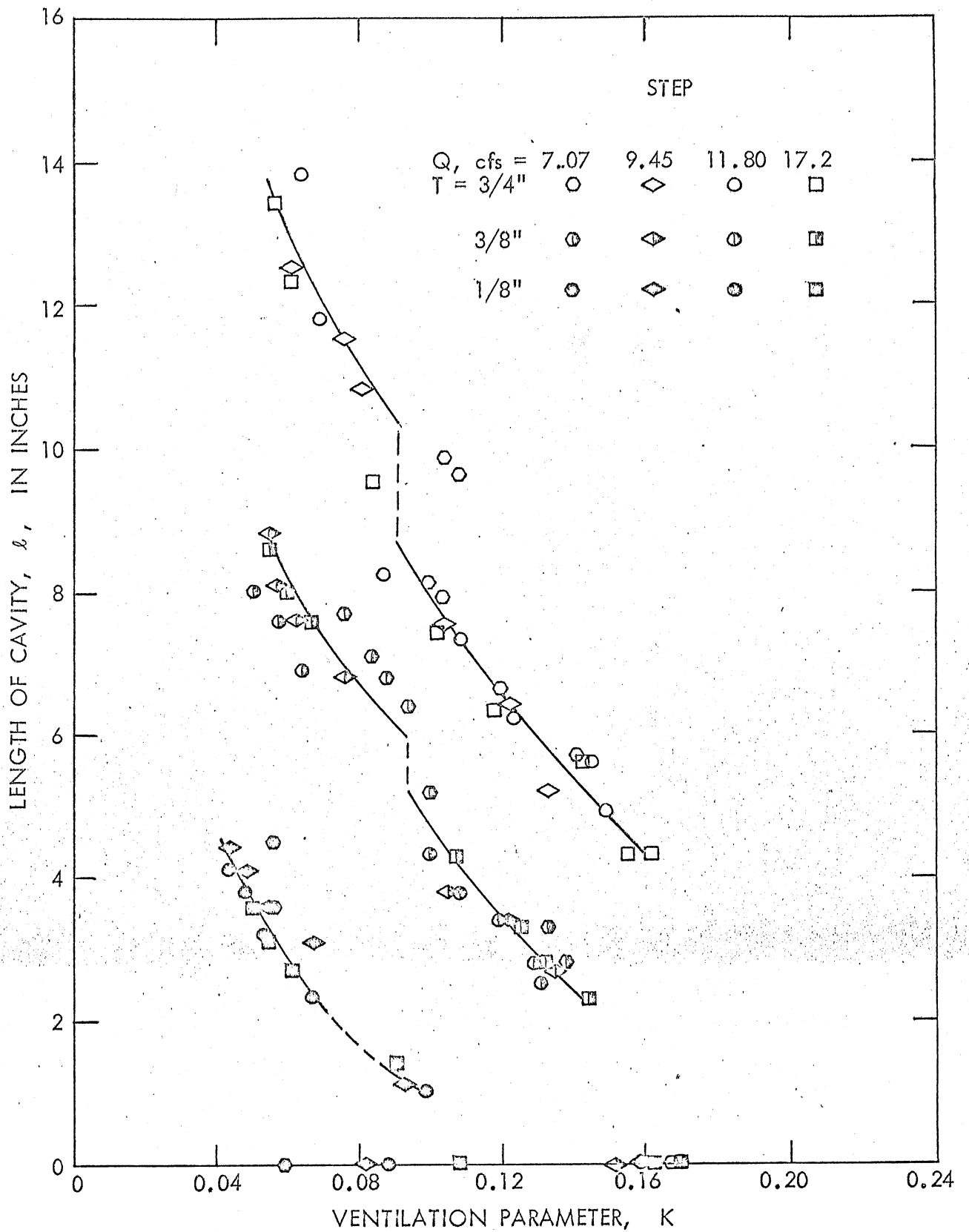


Fig. 12 - Length of Cavity versus Ventilation Parameter for the Step

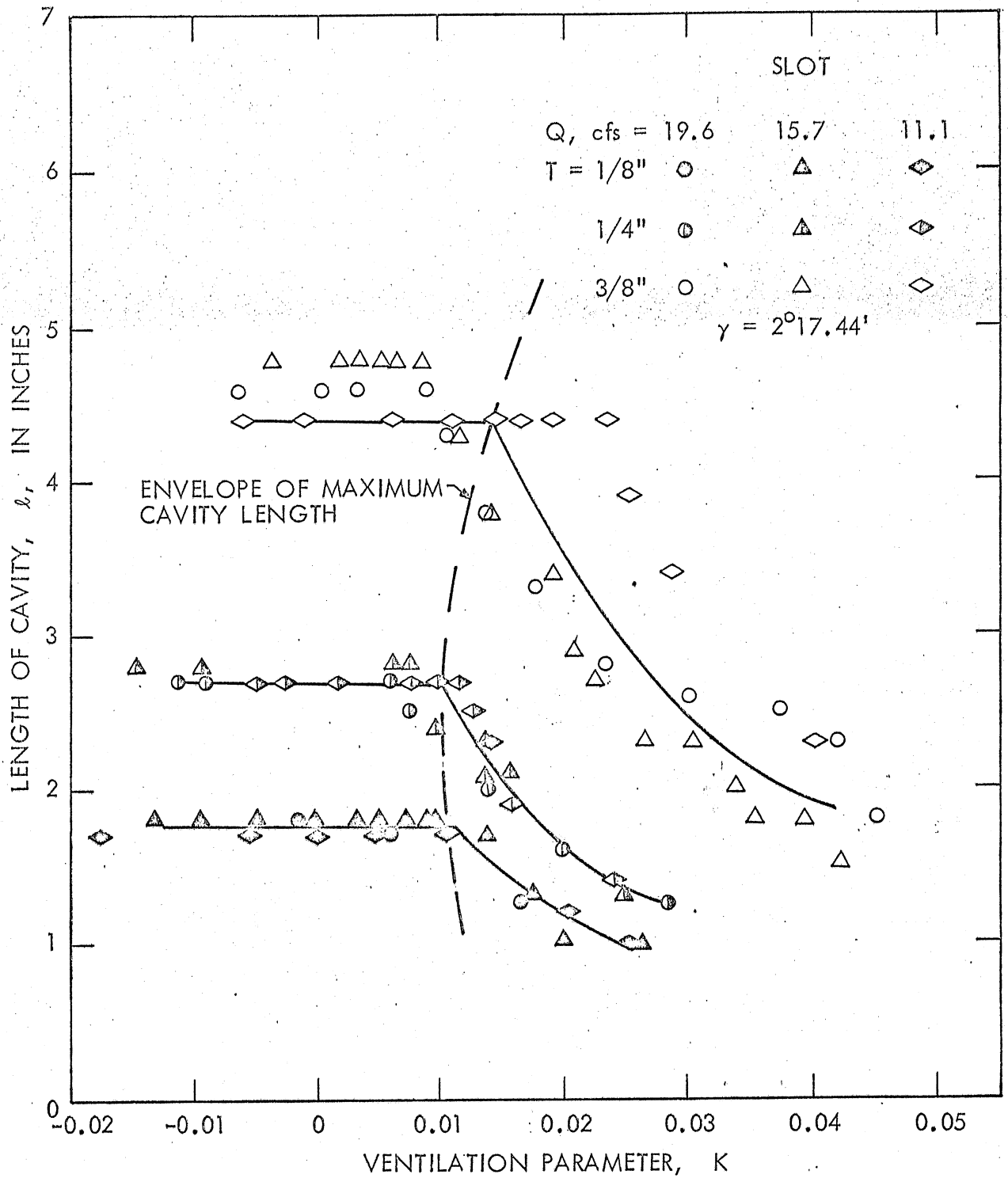


Fig. 13 - Length of Cavity versus Ventilation Parameter for the Slot

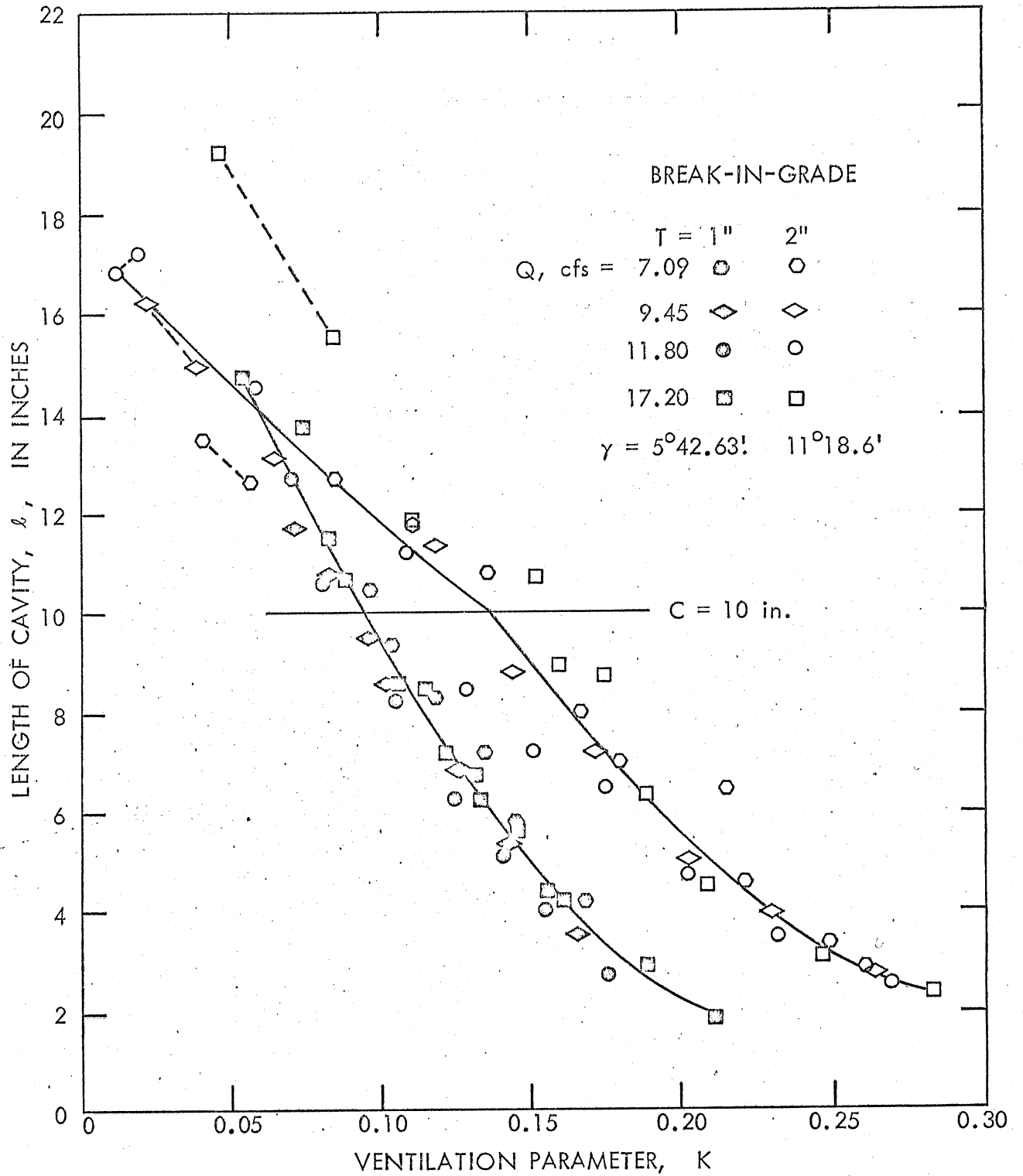


Fig. 14 - Length of Cavity versus Ventilation Parameter for the Break-in-Grade

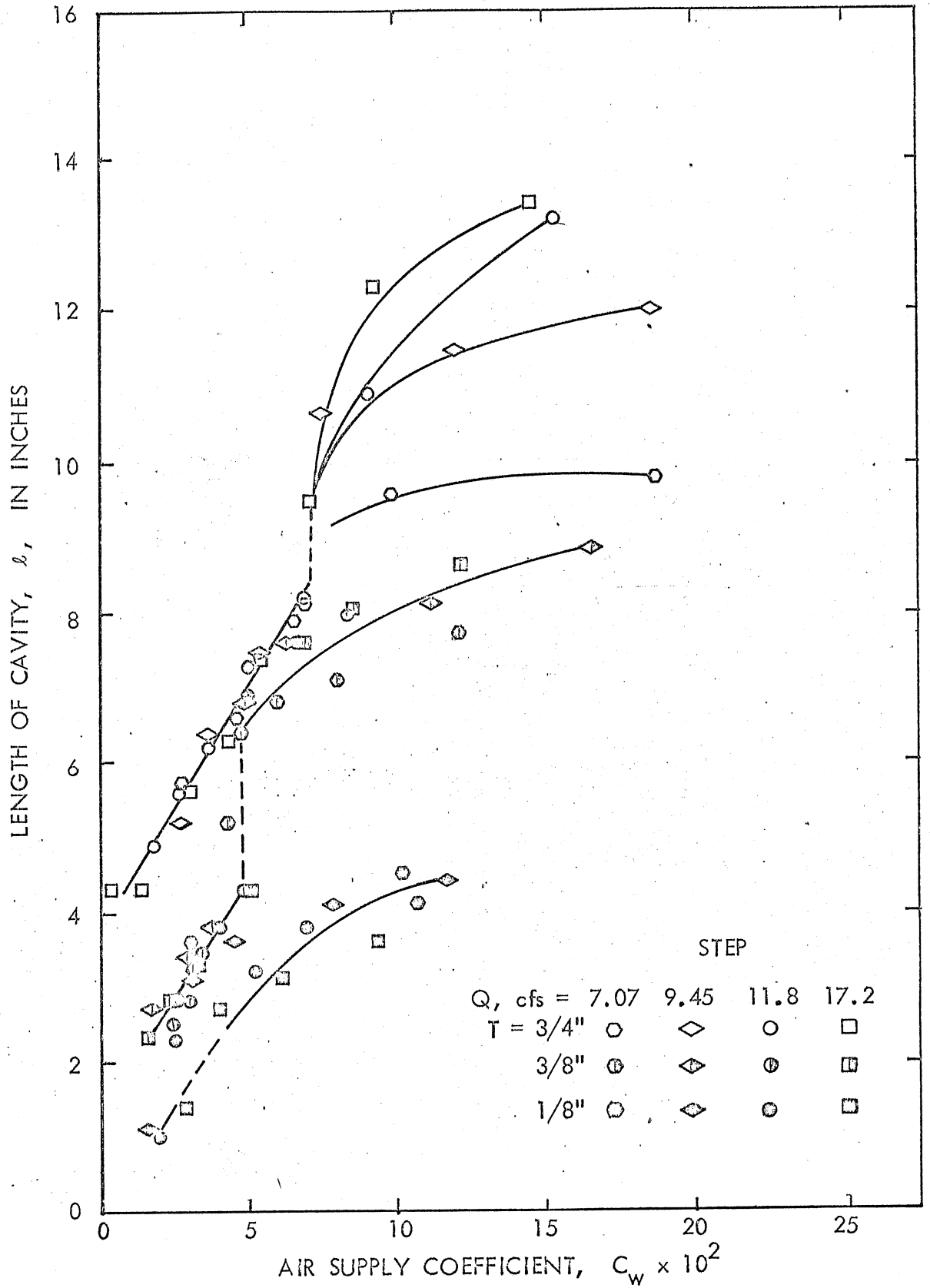


Fig. 15 - Length of Cavity versus Air Supply Coefficient for the Step

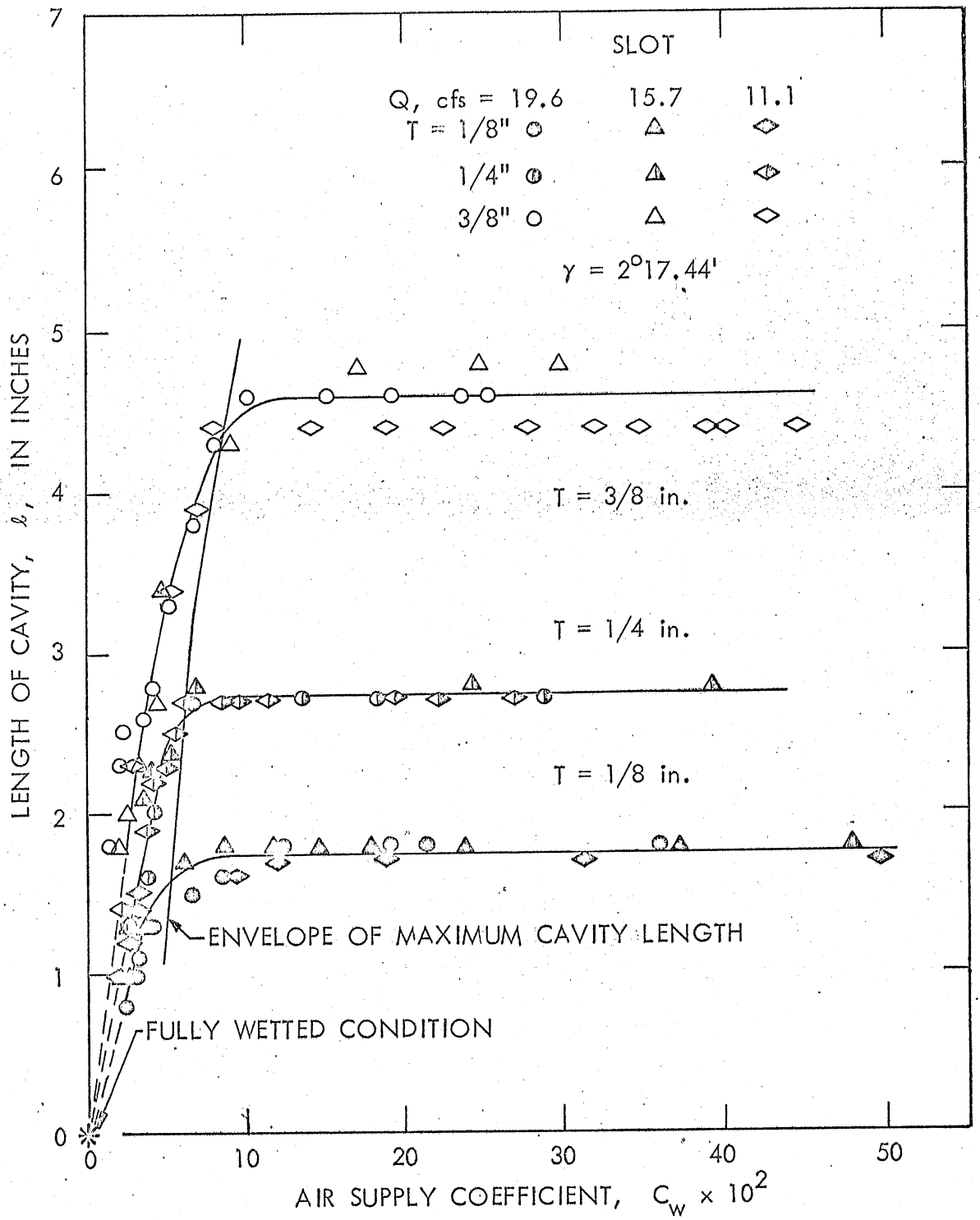


Fig. 16 - Length of Cavity versus Air Supply Coefficient for the Slot

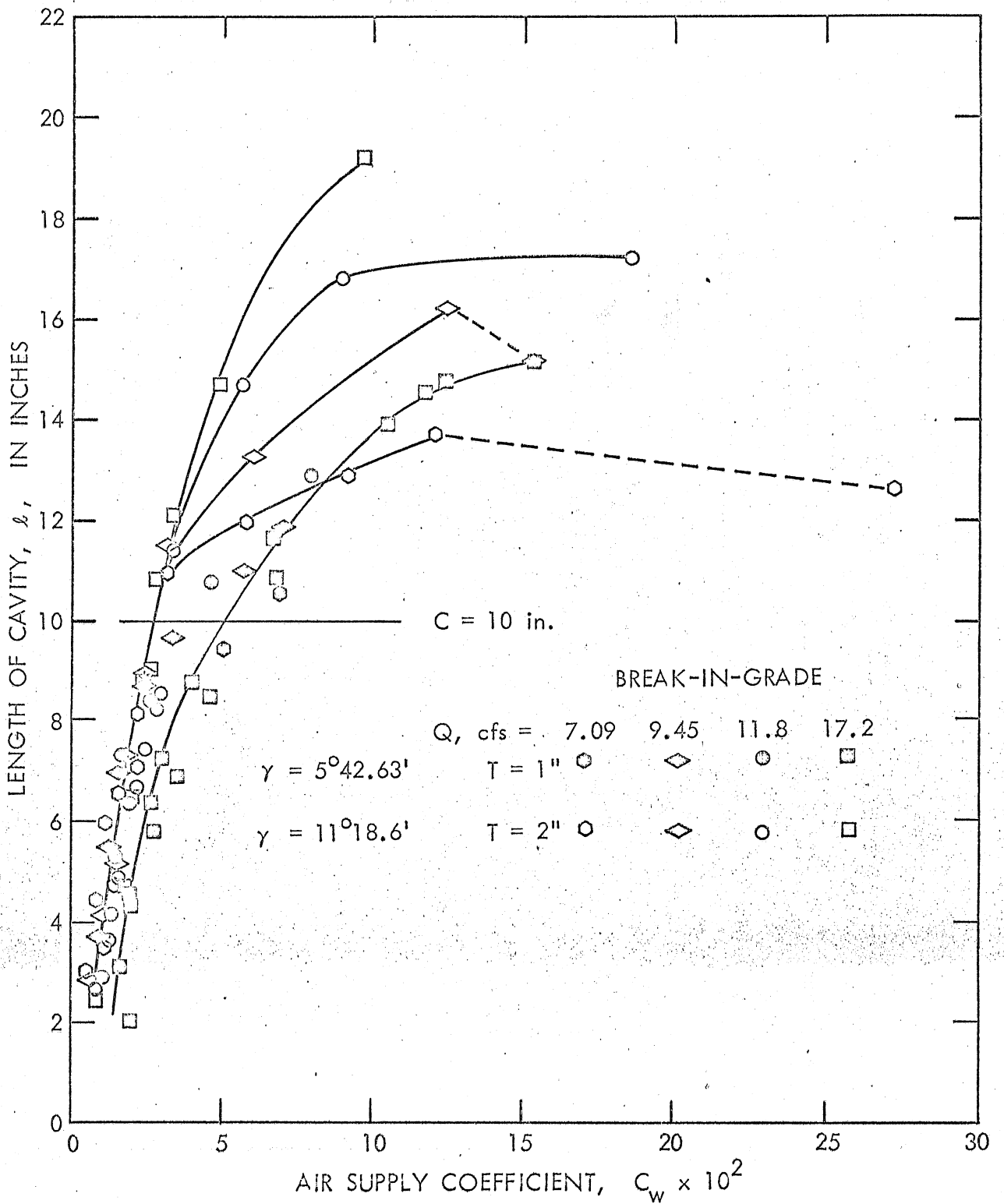


Fig. 17 - Length of Cavity versus Air Supply Coefficient for the Break-in-Grade

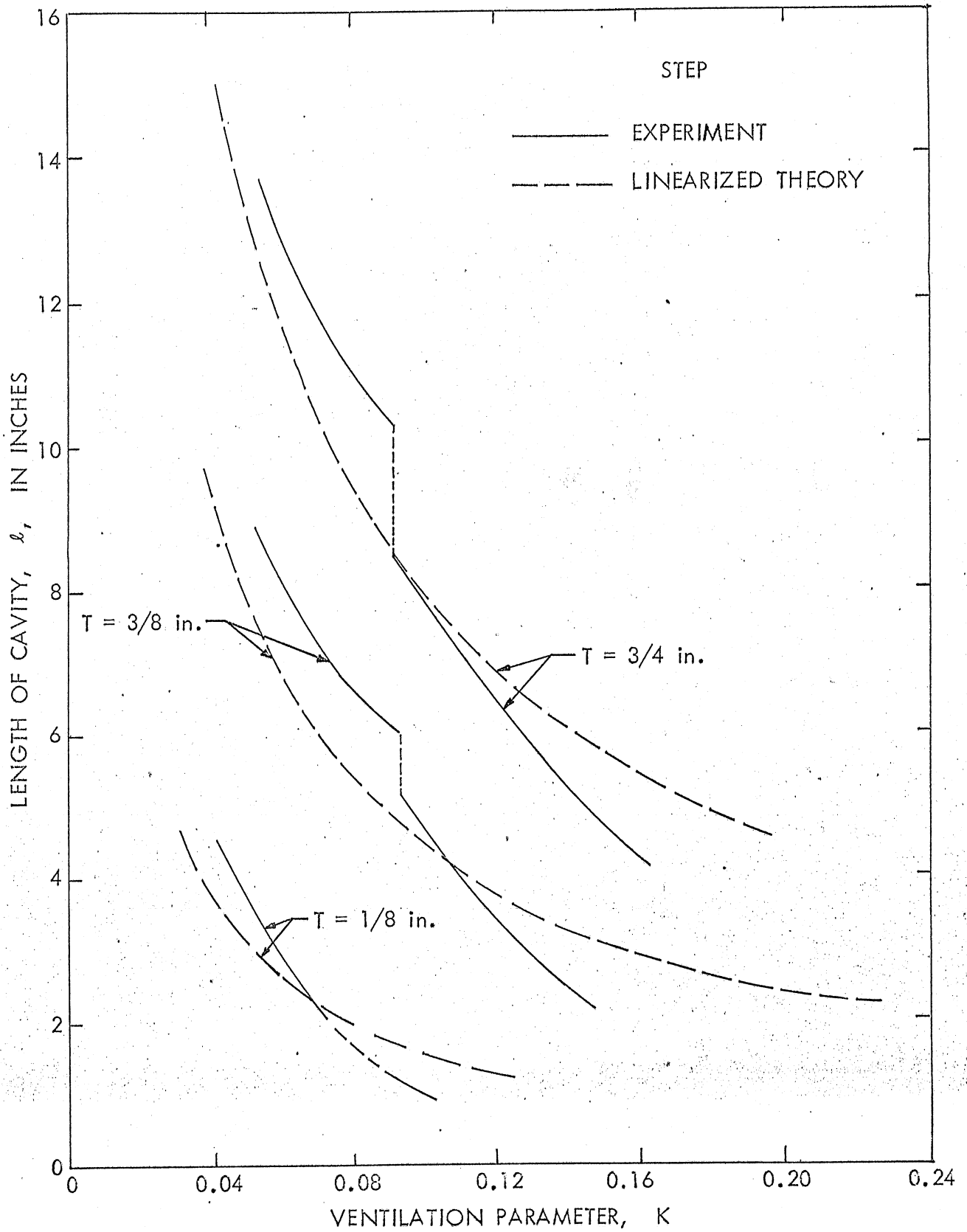


Fig. 18 - Comparison of Experimental Results with Linearized Theory for the Step

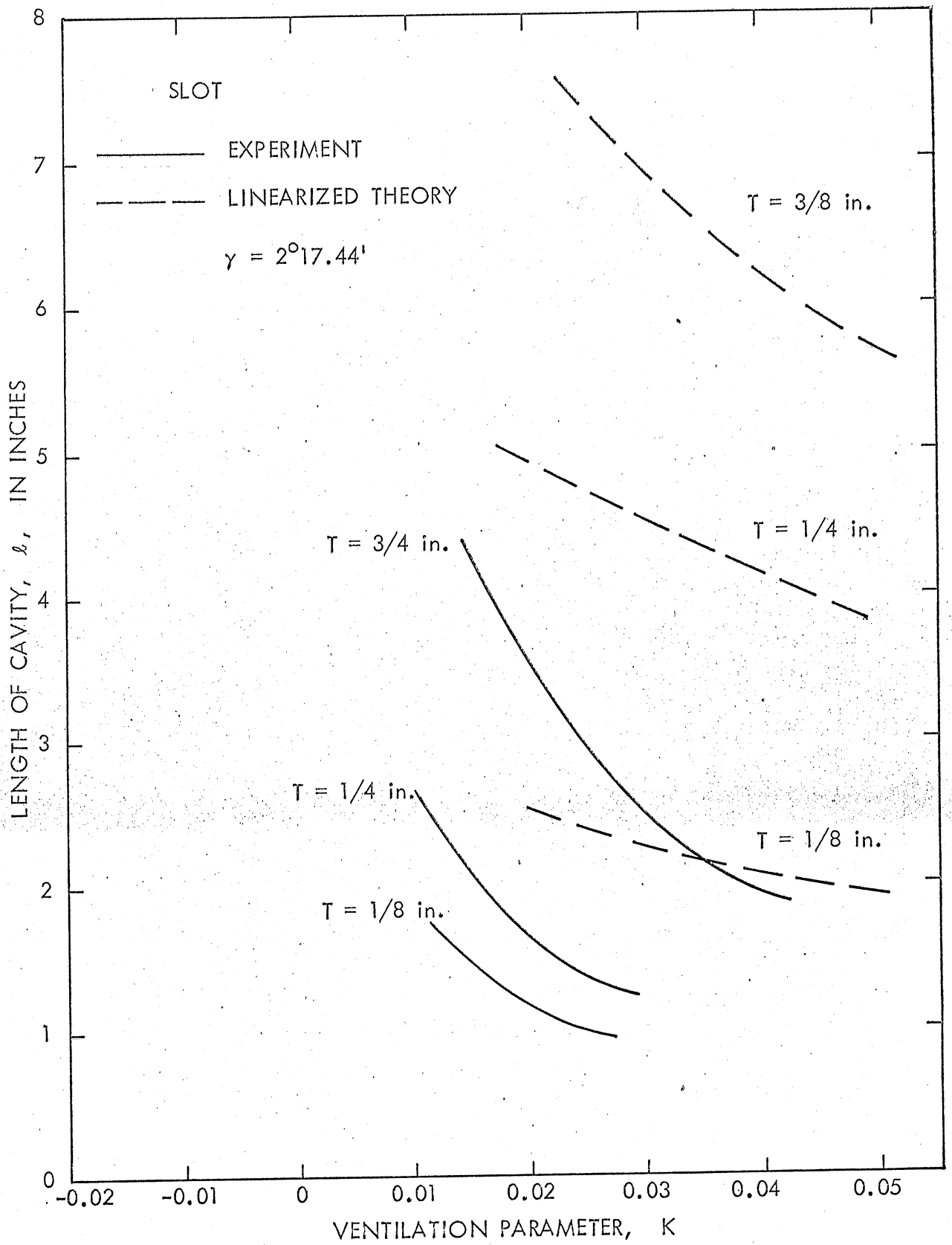


Fig. 19 - Comparison of Experimental Results with Linearized Theory for the Slot

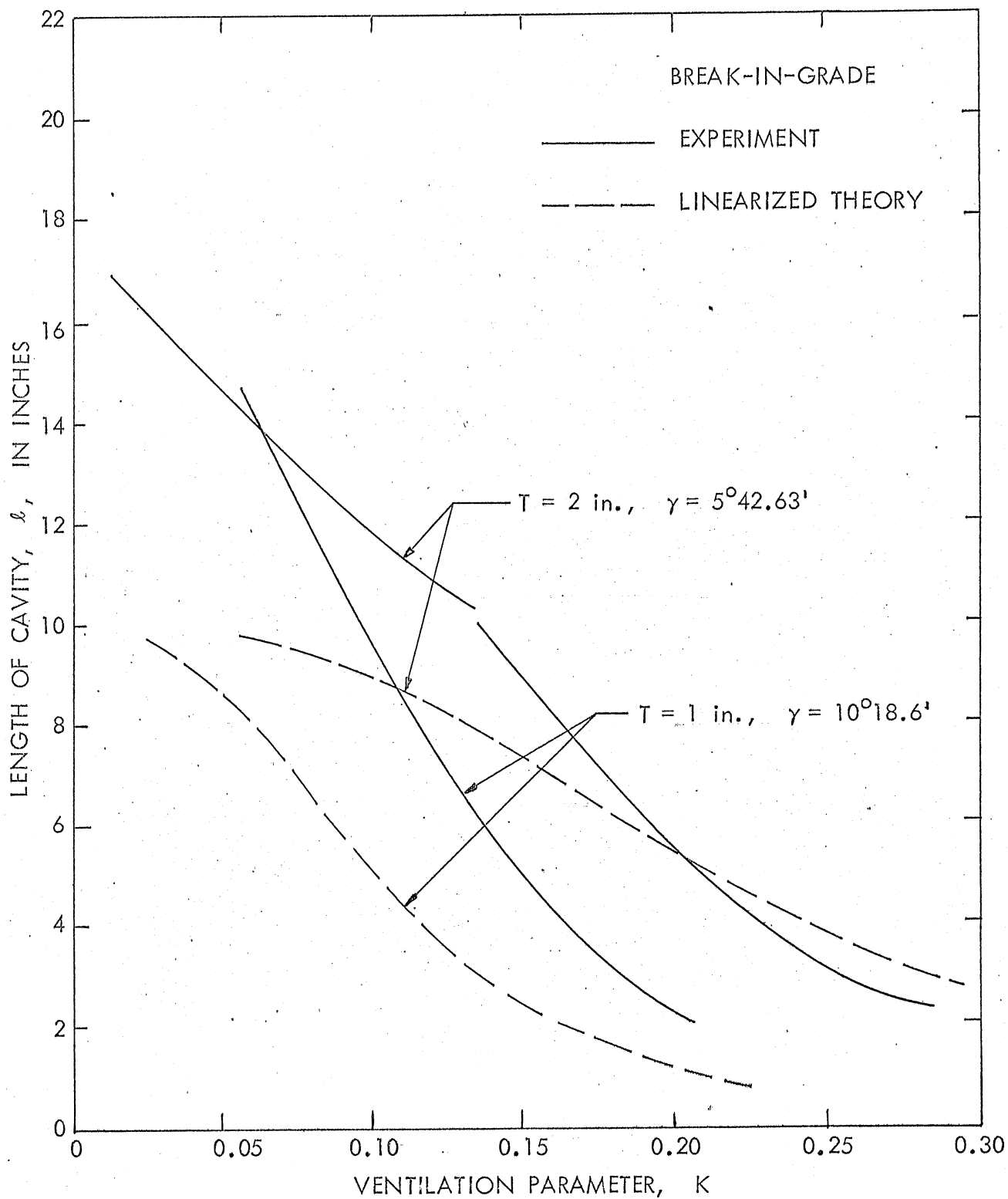


Fig. 20 - Comparison of Experimental Results with Linearized Theory for the Break-in-Grade

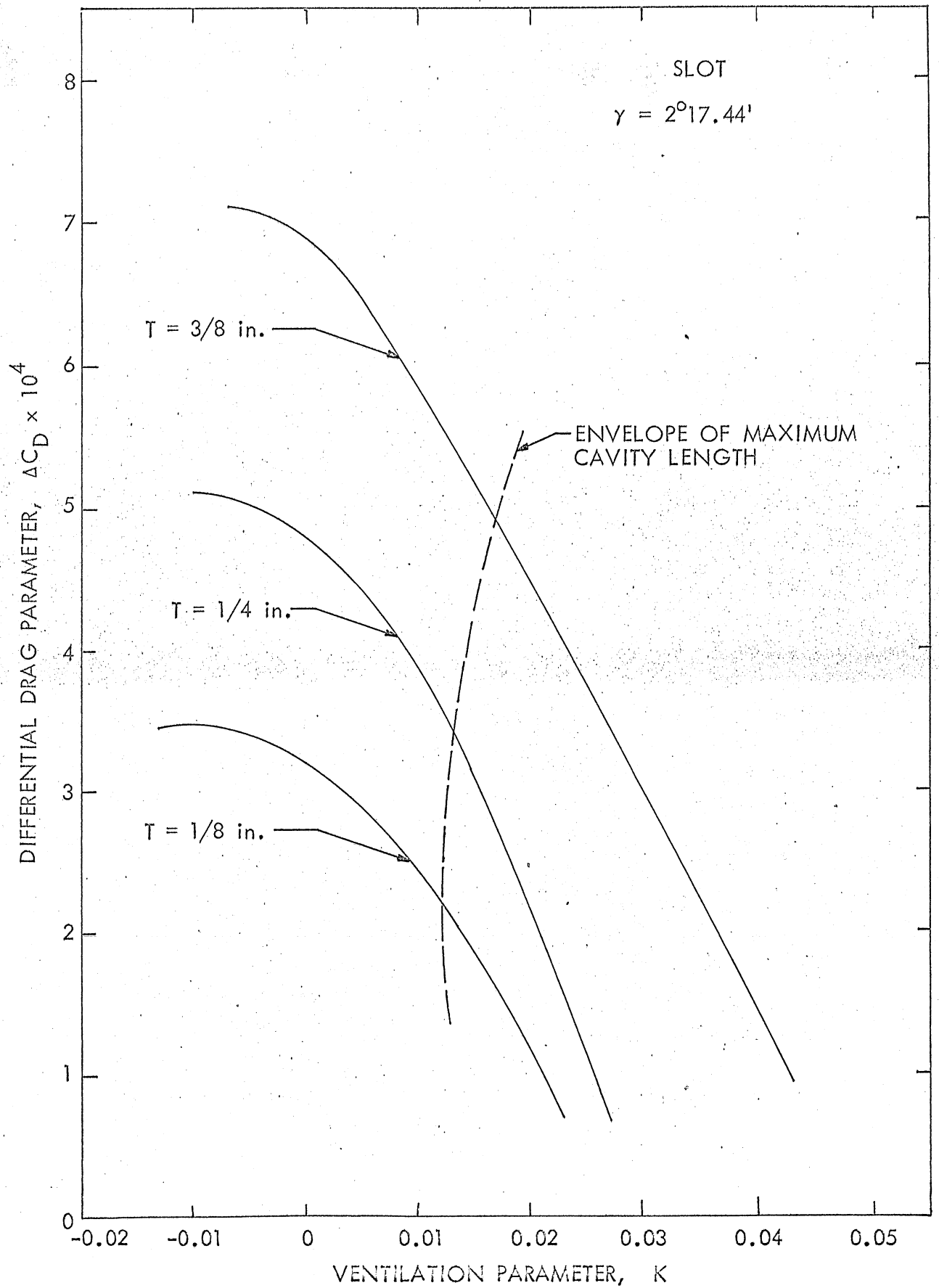


Fig. 21 - Differential Drag Parameter versus Ventilation Parameter for the Slot

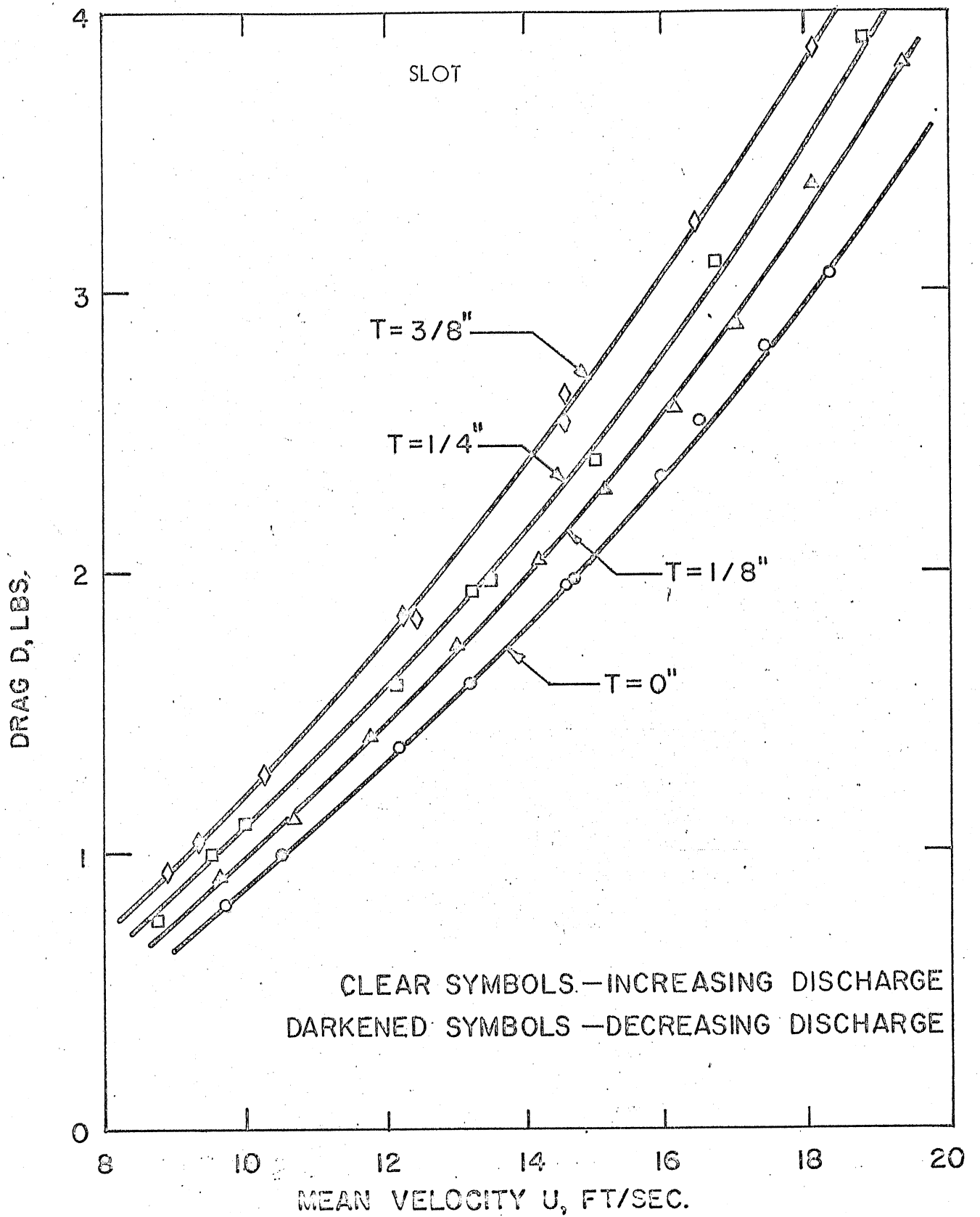


Fig. 22 - Drag Variation with Mean Velocity for the Smooth Plate and the Slot

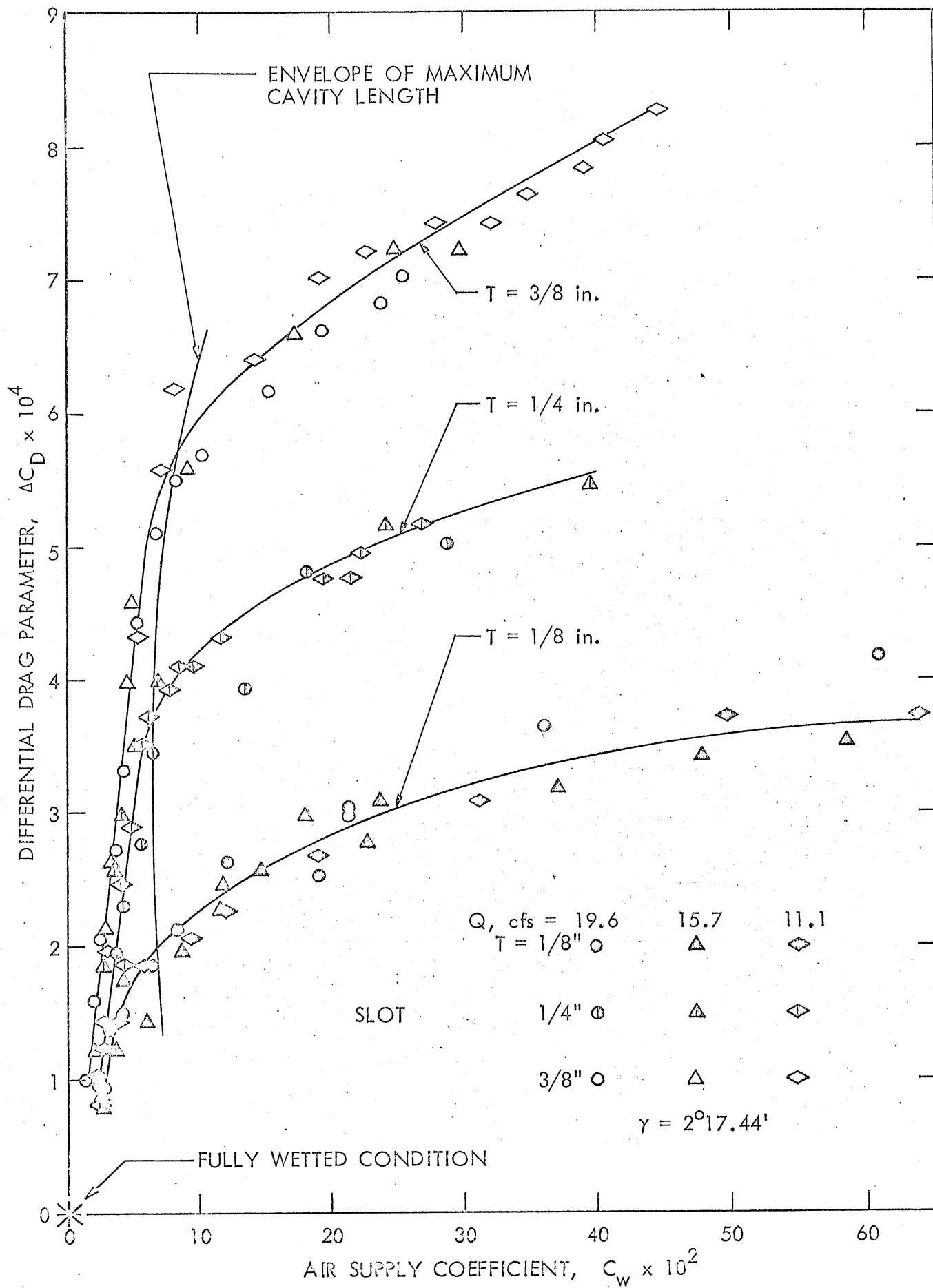


Fig. 23 - Differential Drag Parameter versus Air Supply Coefficient for the Slot

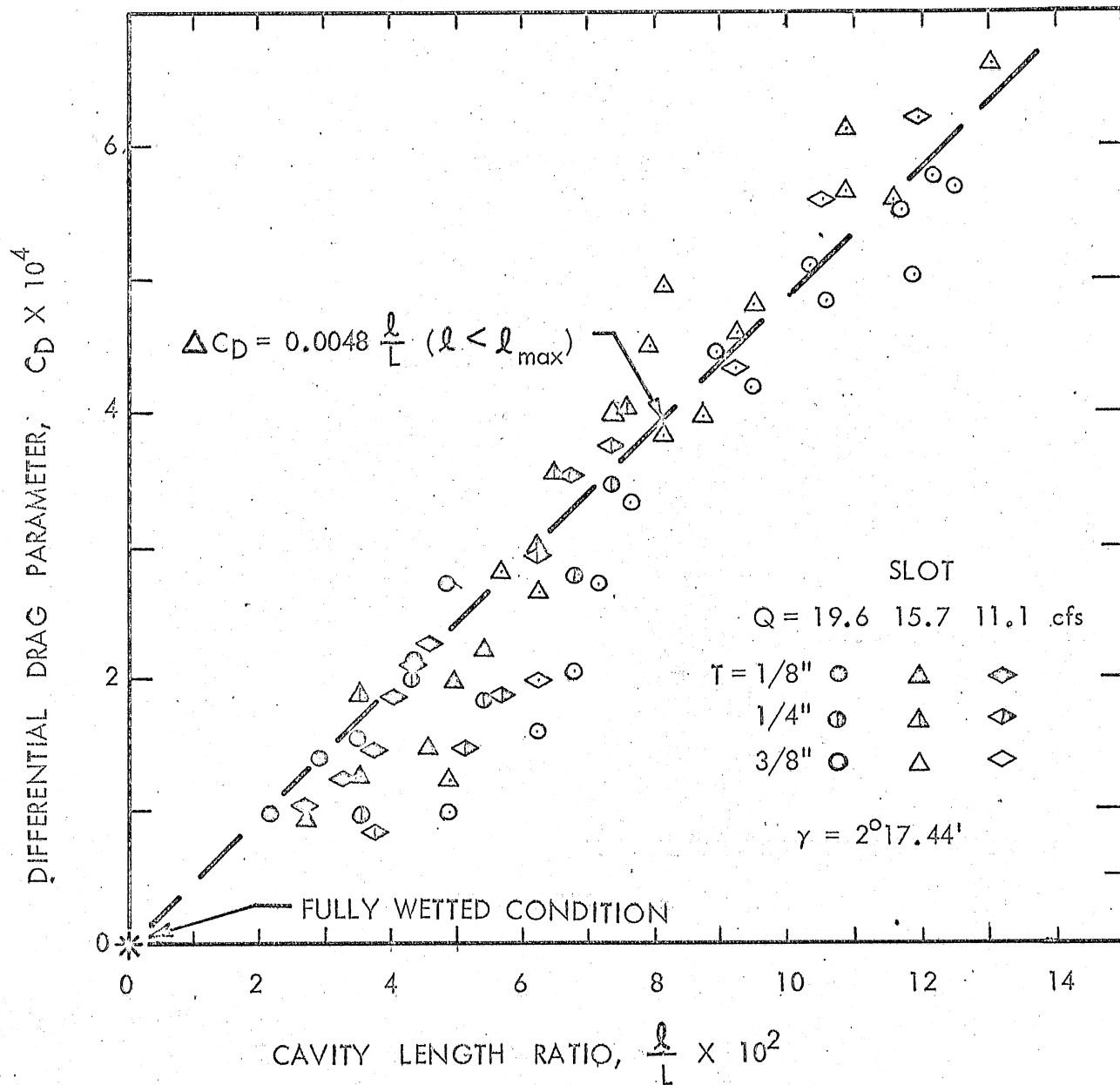


Fig. 24 - Differential Drag Parameter versus Cavity Length Ratio for the Slot

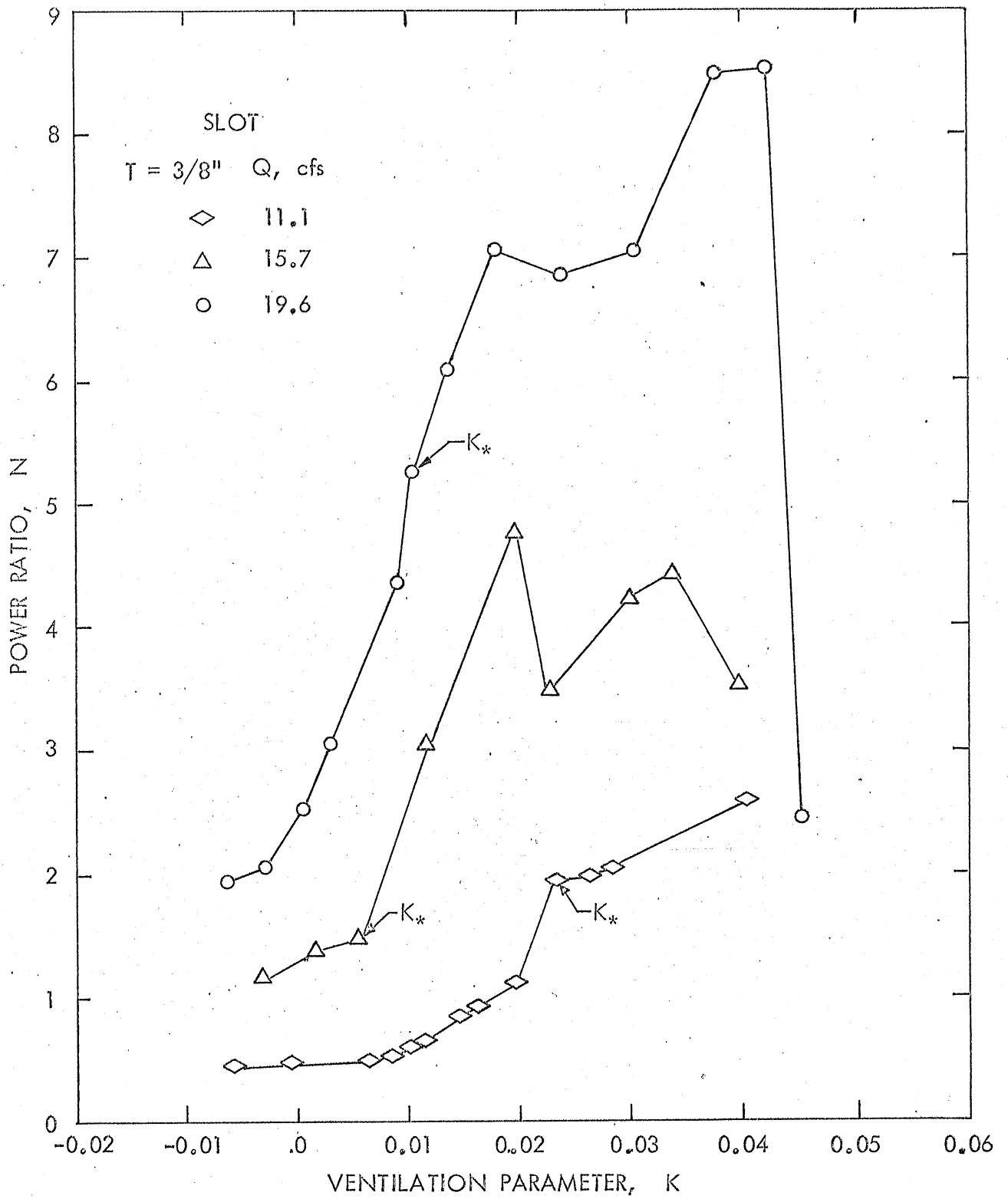


Fig. 25 - Power Ratio versus Ventilation Parameter for the Slot

Appendix -- ANALYSIS

LIST OF SYMBOLS - APPENDIX

$d$	Depth of flow
$E$	Small number
$E(k)$	The complete elliptic integral of the second kind
$F(\phi, k)$	The normal elliptic integral of the first kind
$G(\zeta)$	Analytic function in $\zeta$ -plane
$H(\zeta)$	Homogeneous solution
$I_1$	Integral function
Imag.	Imaginary part of
$K$	Cavitation number
$K(k)$	The complete elliptic integral of the first kind
$k, k_1$	Modulus
$C$	Sloping length of the discontinuous boundary in physical plane
$C'$	Sloping length of the discontinuous boundary in $\zeta$ -plane
$l$	Cavity length
$P$	Pressure at any point
$P_c$	Cavity pressure
$P_R$	Pressure at infinity
Re	Real part of
$U$	Velocity at infinity in x-direction
$U_c$	Velocity on the cavity boundary
$u$	Velocity component in x-direction
$u'$	Dimensionless perturbation velocity in x-direction
$v$	Velocity component in y-direction
$v'$	Dimensionless perturbation velocity in y-direction
$W(z)$	Complex conjugate of perturbation velocity

$X_0$	Reduced depth in $\zeta$ -plane
$z$	Complex variable
$\gamma$	Wedge angle
$\zeta$	Upper half plane
$\eta$	Imaginary axis in $\zeta$ -plane
$\nu$	Imaginary part of complex function $W(\zeta)$
$\mu$	Real part of complex function
$\xi$	Real axis in $\zeta$ -plane
$\rho$	Density
$\tau$	Variable of integration

## Appendix -- ANALYSIS

### A. Linearized Theory

The characteristics of a cavity located in the boundary discontinuities tested can be represented (as an initial approximation) by a linearized model of steady, two-dimensional, irrotational, incompressible flow with finite depth. In the linearized theory the cavity becomes a slit on the x-axis of the physical plane and linearized boundary conditions are satisfied in mapping the break-in-grade, step, and slot configurations. Conformal mapping and complex variable techniques are used to formulate the mixed boundary value problem in establishing the relationship between the cavity length and the cavitation number.

The method given by Cheng and Rott [A-1]<sup>\*</sup> and further extended by Yalamanchili [A-2] is used to reduce the mixed boundary value problem to regular boundary value conditions leading to the solution of a conjugate perturbation velocity. If further effects of gravity and surface tension are neglected, the dimensionless velocity components are defined as

$$\frac{u}{U} = 1 + u' \quad (\text{A-1a})$$

$$\frac{v}{U} = v' \quad (\text{A-1b})$$

where the perturbation components  $u'$  and  $v'$  are shown to satisfy continuity and the conditions of irrotationality. The perturbation velocities are therefore harmonic and the complex conjugate of the perturbation velocities

$$W(z) = u' - iv' \quad (\text{A-2})$$

satisfies Laplace's equation and is an analytic function outside of the body cavity system. The boundary conditions applicable to the real and imaginary parts of  $W(z)$  are established and the solution for  $W(z)$  is obtained.

Boundary flow configurations in the physical and the linearized plane are shown in Figs. A-1, A-2, and A-3 with appropriate boundary conditions.

\*Numbers in brackets refer to the List of References on page A-10.

Linearized theory is applied to facilitate solution of the defining relationships while maintaining the accuracy needed for comparison with experimental results. The basic assumption of linear theory is that a slender body-cavity system causes only small perturbations in the velocity components of the basic flow. Other assumptions inherent in the linear analysis are as follows:

1. The higher order perturbation velocity components are neglected.
2. Perturbation velocities are small compared to unity (i.e.,  $u' \ll 1$ ,  $v' \ll 1$ ).
3. Streamline curvature is mild.
4. Linearized boundary conditions are applied on the horizontal slit representing the cavity in the physical plane.
5. The pressure difference  $P_R - P_C$  is small compared to  $\rho U^2/2$  (i.e., the ventilation parameter is small).
6. Cavity pressure is continuous across the boundary and constant throughout.
7. The pressure in the free stream is nowhere less than the cavity pressure.
8. The free surface is parallel to the solid surface.

The linearized boundary conditions can now be written for the three boundary geometries and the governing equations developed.

#### B. Break-in-Grade

The boundary conditions existing in the break-in-grade flow case are enumerated, with reference to Fig. A-1, as follows:

1. On the free surface  $BO'$  over the discontinuity, the velocity is parallel to the solid boundary and  $u' = \cos \gamma - 1$ .
2. Neglecting higher order terms the boundary conditions on the remaining free surface give  $u' = 0$ .
3. For the upstream solid boundary  $DO$  the vertical velocity perturbation  $v'$  is equal to zero.
4. The cavity  $OE$  is characterized by  $u' = K/2$ . This can be shown by combining the Bernoulli equation with the definition of the cavitation number as follows:

$$P_R + \rho U^2/2 = P_c + \rho U_c'^2/2 \quad (A-3)$$

where

$$K = \frac{P_R - P_c}{\rho U^2/2} \quad (A-4)$$

Combining Eqs. (A-3) and (A-4) gives

$$K = \frac{P_R - P_c}{\rho U^2/2} = \frac{U_c'^2}{U^2} - 1 \quad (A-5)$$

where the subscript  $c$  refers to cavity conditions.

Considering Eqs. (A-1a) and (A-1b) and neglecting higher order terms, Eq. (A-5) can be rewritten as

$$K = (1 + u_c')^2 + v_c'^2 - 1$$

which reduces to  $u_c' = K/2$ .

5. Where the velocity is parallel to the boundary of EF,

$$\tan \gamma = \frac{v'}{1 + u'} \approx v' \quad \text{for } u' \ll 1$$

6. On FG,  $v' = 0$  and at infinity both  $u'$  and  $v'$  equal zero.

The break-in-grade solution is obtained by using Schwarz-Christoffel transformation where the flow in the linearized  $z$ -plane is transformed onto the  $\zeta$ -plane as shown in Fig. A-1. The transformation functions are given as

$$\zeta = X_0 [e^{\pi z/d} - 1] \quad (A-6)$$

and

$$C' = X_0 [e^{\pi C/d} - 1] \quad (A-7)$$

where

$$X_0 = \ell / [e^{\pi \ell/d} - 1]$$

The flow in the  $\zeta$ -plane forms a mixed boundary value problem which is solved by reducing to a regular boundary value problem where the imaginary part is known on the entire real axis. An analytic function  $G(\zeta)$  is then defined as

$$G(\zeta) = \frac{W(\zeta)}{H(\zeta)} = \mu(\xi, \eta) - i\nu(\xi, \eta) \quad (\text{A-8})$$

where

$$H(\zeta) = \sqrt{(\zeta + X_0) \zeta(\zeta - l)}$$

The transformed boundary conditions of  $G(\zeta)$  can now be written as

1. On AB,  $v = 0$
2. On BO',  $v = i \frac{\cos \gamma - 1}{H(\zeta)}$
3. On O'C,  $v = 0$
4. On DO,  $v = 0$
5. On OE,  $v = i \frac{K/2}{H(\zeta)}$
6. On EF,  $v = -\frac{\tan \gamma}{H(\zeta)}$
7. On FG,  $v = 0$
8. At infinity,  $u' = 0, v' = 0$

Thus the imaginary part of the function  $G(\zeta)$  is specified on the entire real axis. For a finite break-in-grade length the boundary condition at infinity is  $u' = 0$  and the general solution for  $W(\zeta)$  becomes

$$W(\zeta) = 0 = -\frac{K}{2} \int_0^l \frac{d\tau}{\sqrt{(\tau + X_0) \tau(\tau - l)}} + \tan \gamma \int_l^{C'} \frac{d\tau}{\sqrt{(\tau + X_0) \tau(\tau - l)}} \\ \pm 2(1 - \cos \gamma) \left[ \int_{-\infty}^{-2X_0} \frac{d\tau}{\sqrt{(\tau + X_0) \tau(\tau - l)}} - \int_{-\infty}^B \frac{d\tau}{\sqrt{(\tau + X_0) \tau(\tau - l)}} \right] \quad (\text{A-9})$$

where  $B = X_0 [e^{\pi C/d} + 1]$ .

Integration of Eq. (A-9) can be written as follows:

$$K = \frac{2 \tan \gamma F(\phi_1, k_1) \pm 2(1 - \cos \gamma)[F(\phi_2, k_2) - F(\phi_3, k_3)]}{K(k_4)} \quad (\text{A-9a})$$

where

$$\phi_1 = \sin^{-1} \sqrt{(C' - \ell)/C'}, \quad \phi_2 = \sin^{-1} \sqrt{(\ell + X_0)/(\ell + 2X_0)}$$

$$\phi_3 = \sin^{-1} \sqrt{(\ell + X_0)/(\ell + B)}, \quad k_1 = \sqrt{X_0/(\ell + X_0)}$$

$$k_2 = k_3 = k_4 = \sqrt{\ell/(\ell + X_0)}$$

$$B = X_0(e^{\pi \ell/d} + 1), \quad C' = X_0(e^{\pi C/d} - 1)$$

$$X_0 = \ell/(e^{\pi \ell/d} - 1)$$

When C is set equal to unity, the form of the dimensionless solution for Eq. (A-9) becomes

$$K = \frac{2 \tan \gamma F(\phi_1, k_1) \pm 2(1 - \cos \gamma)[F(\phi_2, k_2) - F(\phi_3, k_3)]}{K(k_4)} \quad (\text{A-10})$$

where

$$\phi_1 = \sin^{-1} \sqrt{(C'' - \ell/C)/C''}, \quad \phi_2 = \sin^{-1} \sqrt{(\ell/C + X_0'')/(\ell/C + 2X_0'')},$$

$$\phi_3 = \sin^{-1} \sqrt{(\ell/C + X_0'')/(\ell/C + B'')}, \quad k_1 = \sqrt{X_0''/(\ell/C + X_0'')},$$

$$k_2 = k_3 = k_4 = \sqrt{(\ell/C)/(\ell/C + X_0'')}$$

$$B'' = X_0''(e^{\pi C/d} - 1), \quad C'' = X_0''(e^{\pi C/d} - 1)$$

$$X_0'' = (\ell/C)/(e^{\pi \ell/d} - 1)$$

## C. Step

A cavity located at a step of thickness  $T$  is considered in much the same manner as was the previous case. Figure A-2 gives the flow configuration in the physical and linearized planes with the boundary conditions indicated.

The linearized boundary conditions for the step can be written as

1. On AO'B, Free Surface,  $u' = 0$
2. On CO, Solid Boundary,  $v' = 0$
3. On OD, Cavity,  $u' = K/2$
4. At infinity,  $u' = 0, v' = 0$
5. Closure conditions:  $-\text{Imag.} \int_0^l W(z) dz = -T$

Following the same procedure set up in the break-in-grade case,

$$G(\zeta) = \frac{W(\zeta)}{H(\zeta)} = \mu - iv$$

where

$$H(\zeta) = \sqrt{\frac{(\zeta)(\zeta + X_0)}{(\zeta - l)}}$$

The boundary conditions for  $G(\zeta)$  can now be given as

1. On OA,  $v = 0$
2. On CO,  $v = 0$
3. On OD,  $v = i \frac{K/2}{H(\zeta)}$
4. On DE,  $v = 0$
5. At infinity,  $v = 0$
6. Closure conditions:  $\text{Imag.} \int_0^l W(z) dz = T$

$$\text{Imag.} \int_0^l \frac{W(\xi) d\xi}{\xi + X_0} \frac{d}{\pi} = T$$

The imaginary part of the function  $G(\zeta)$  is specified on the entire real axis. The general solution for  $W(\xi)$  can be written in dimensionless form as

$$K = \frac{\pi}{d} \frac{2 \ell/T + X'_0}{\ell/T} [K(k_1)]^2 \quad (\text{A-11})$$

where

$$k_1 = \sqrt{\frac{\ell/T}{\ell/T + X'_0}}$$

and

$$X'_0 = \frac{\ell/T}{(e^{\pi \ell/d} - 1)}$$

#### D. Slot

A closed cavity exists starting at the breaking point of a slot of thickness  $T$  in a boundary, as shown in Fig. A-3. Boundary conditions for the linearized case are

1. On AB, Free Surface,  $u' = 0$
2. On CO, Solid Surface,  $v' = 0$
3. On OD, Cavity,  $u' = K/2$
4. On DE,  $v' = \tan \gamma$
5. On EF,  $v' = 0$
6. At infinity,  $u' = 0, v' = 0$
7. Closure conditions:  $\text{Imag.} \int_0^{\ell} W(z) dz = \frac{T}{C} (C - \ell)$

The analytical function  $G(\zeta)$  is defined as

$$G(\zeta) = \frac{W(\zeta)}{H(\zeta)} = \mu - i\nu$$

where

$$H(\zeta) = \sqrt{\frac{(\zeta + X'_0)(\zeta)}{(\zeta - \ell)}}$$

The boundary conditions for  $G(\zeta)$  in this case are

1. On AB,  $v = 0$
2. On BO,  $v = 0$
3. On OD,  $v = \frac{iK/2}{H(\zeta)}$
4. On DE,  $v = \tan \gamma / H(\zeta)$
5. On EF,  $v = 0$
6. Closure conditions:  $\text{Imag} \frac{d}{d\xi} \int_0^{\ell} W(\xi) \frac{d\xi}{(\xi + X_0)} = \frac{T}{C} (C - \ell)$

Again the imaginary part of the function  $G(\zeta)$  is specified on the entire real axis, and the general solution for  $W(\zeta)$ , using the closure condition, can be written

$$K = \frac{(d/C\pi^2) \tan \gamma I_1 \pm T/C(1 - \ell/C)}{\frac{d/C}{\pi^2} \frac{\ell/C}{\ell/C + X_0} [K(k_1)]^2} \quad (\text{A-12})$$

where

$$I_1 = \left[ \frac{2\ell/C}{k_1^2 \sqrt{\ell/C + X_0}} \left[ E(k_1) - (k_1')^2 K(k_1) \right] \frac{2F(\phi_2, k_2)}{\sqrt{\ell/C + X_0}} \right. \\ \left. - \frac{2}{\sqrt{(\ell/C)(\ell/C + X_0)}} \int_0^{\ell/C} \sqrt{\frac{\xi}{(\xi + X_0)}} \tan^{-1} \sqrt{\frac{E'}{\ell/C - \xi}} d\xi \right. \\ \left. - \int_0^{\ell/C} \sqrt{\frac{\xi(\ell/C - \xi)}{\xi + X_0}} \int_{\ell/C+E}^{C''} \frac{d\tau}{(\tau - \xi) \sqrt{\tau(\tau + X_0)(\tau - \ell/C)}} d\xi \right]$$

where  $X_0 = (\ell/C)/(e^{\pi\ell d} - 1)$

$k_1^2 = (\ell/C)/(\ell/C + X_0)$

$$(k_1')^2 = 1 - k_1^2, \quad E = 0.01, \quad E' = E/C$$

$$\phi_2 = \sin^{-1} \sqrt{(C'' - l/C)/C''}$$

$$k_2 = \sqrt{X_0'/(l/C + X_0')}$$

$$C'' = X_0'(e^{\pi C/d} - 1)$$

## LIST OF REFERENCES - APPENDIX

- [A-1] Cheng, H. K. and Rott, N., "Generalization of the Inversion Formula of Thin Airfoil Theory," Journal of Rational Mechanics and Analysis, Vol. 3, No. 3, 1954.
- [A-2] Yalamanchili, K., "A Linearized Theory for Potential and Rotational Supercavitating Flow over a Wedge in a Two-Dimensional Open Channel," Ph.D. Dissertation, Department of Civil Engineering, University of Minnesota, May, 1965.

LIST OF FIGURES - APPENDIX

FIGURE A-1 Flow Configuration near the Break-in-Grade

FIGURE A-2 Flow Configuration near the Step

FIGURE A-3 Flow Configuration near the Slot

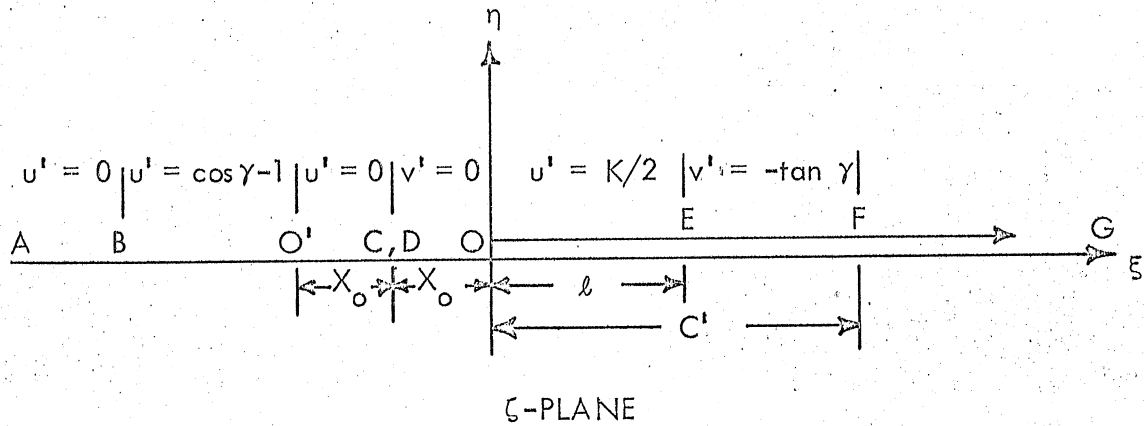
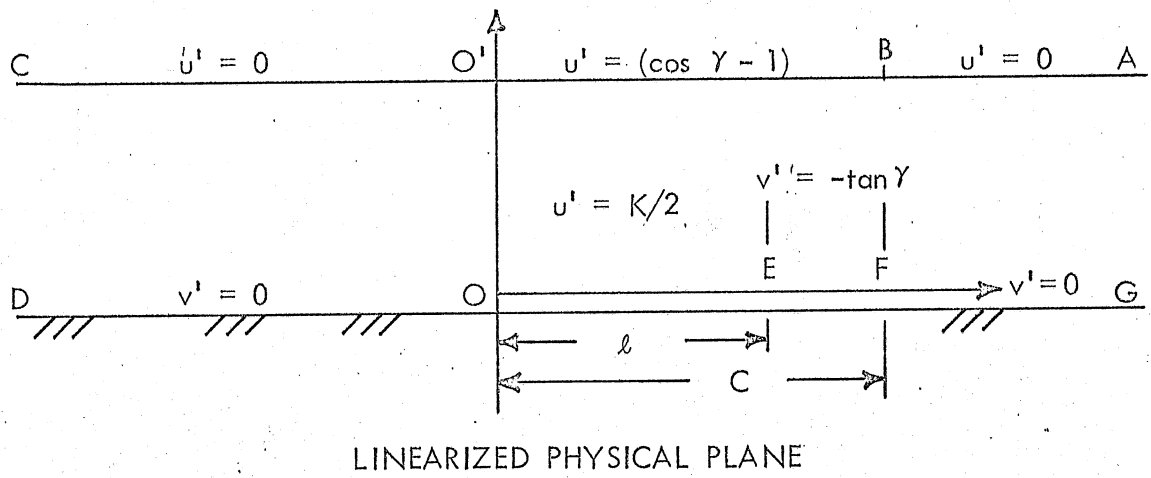
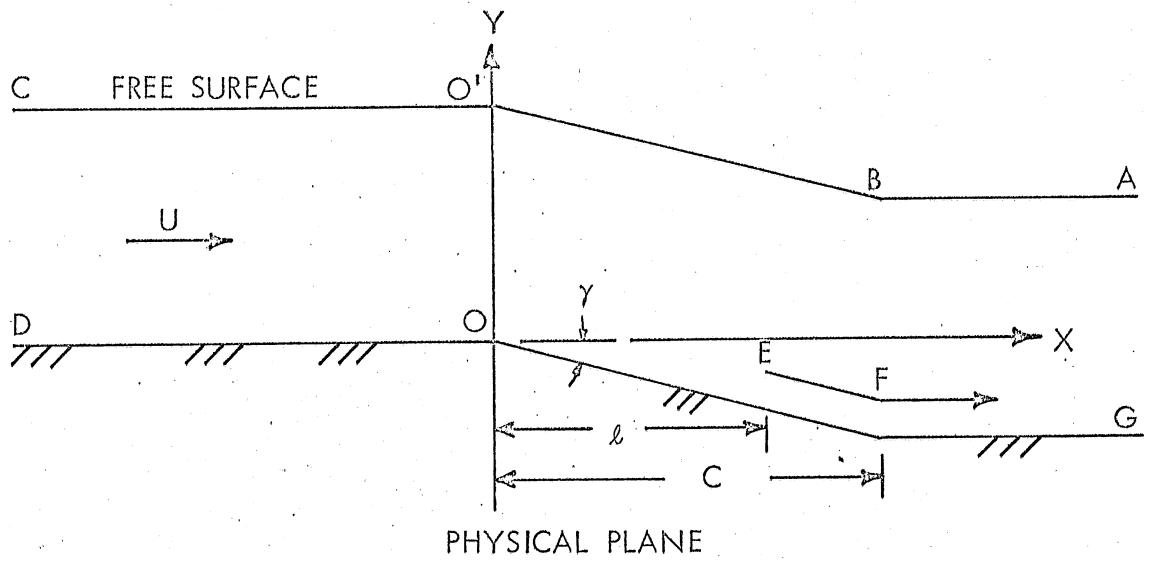
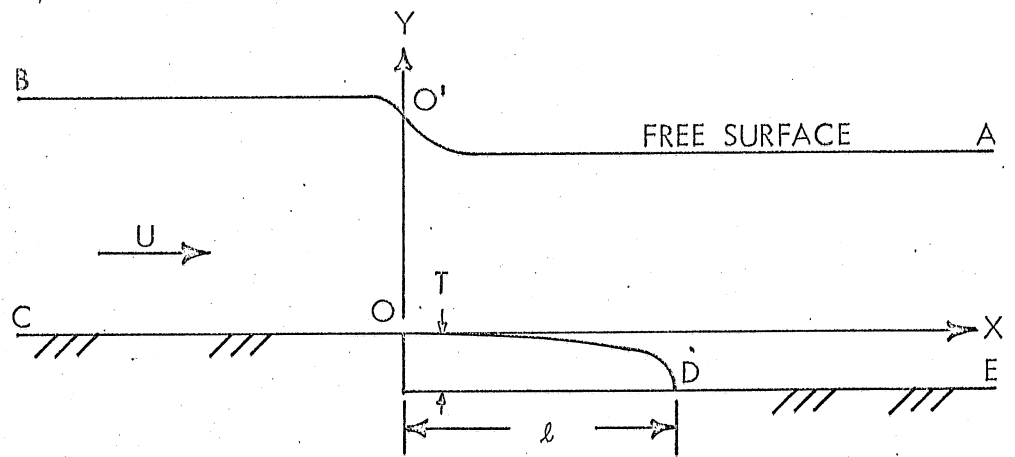
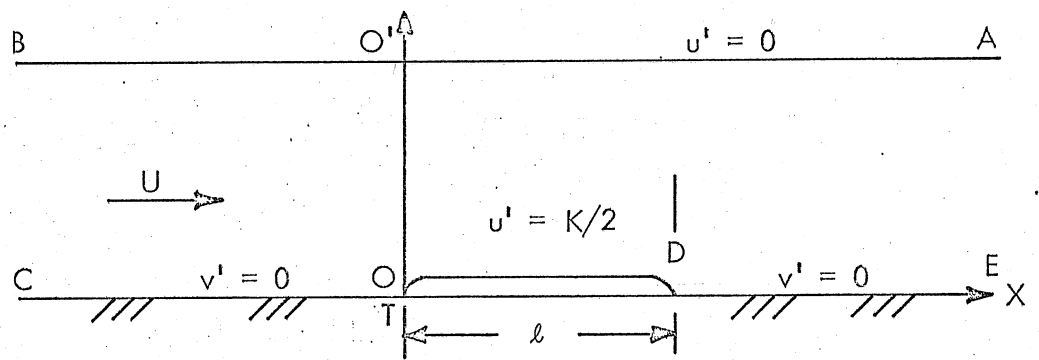


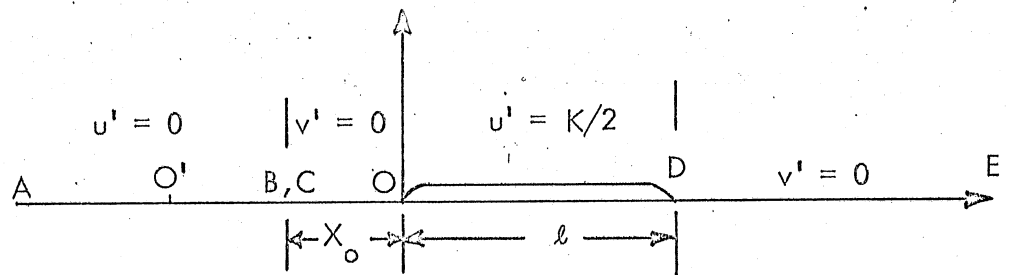
Fig. A-1 - Flow Configuration near the Break-in-Grade



PHYSICAL PLANE



LINEARIZED PHYSICAL PLANE



$\zeta$ -PLANE

Fig. A-2 - Flow Configuration near the Step

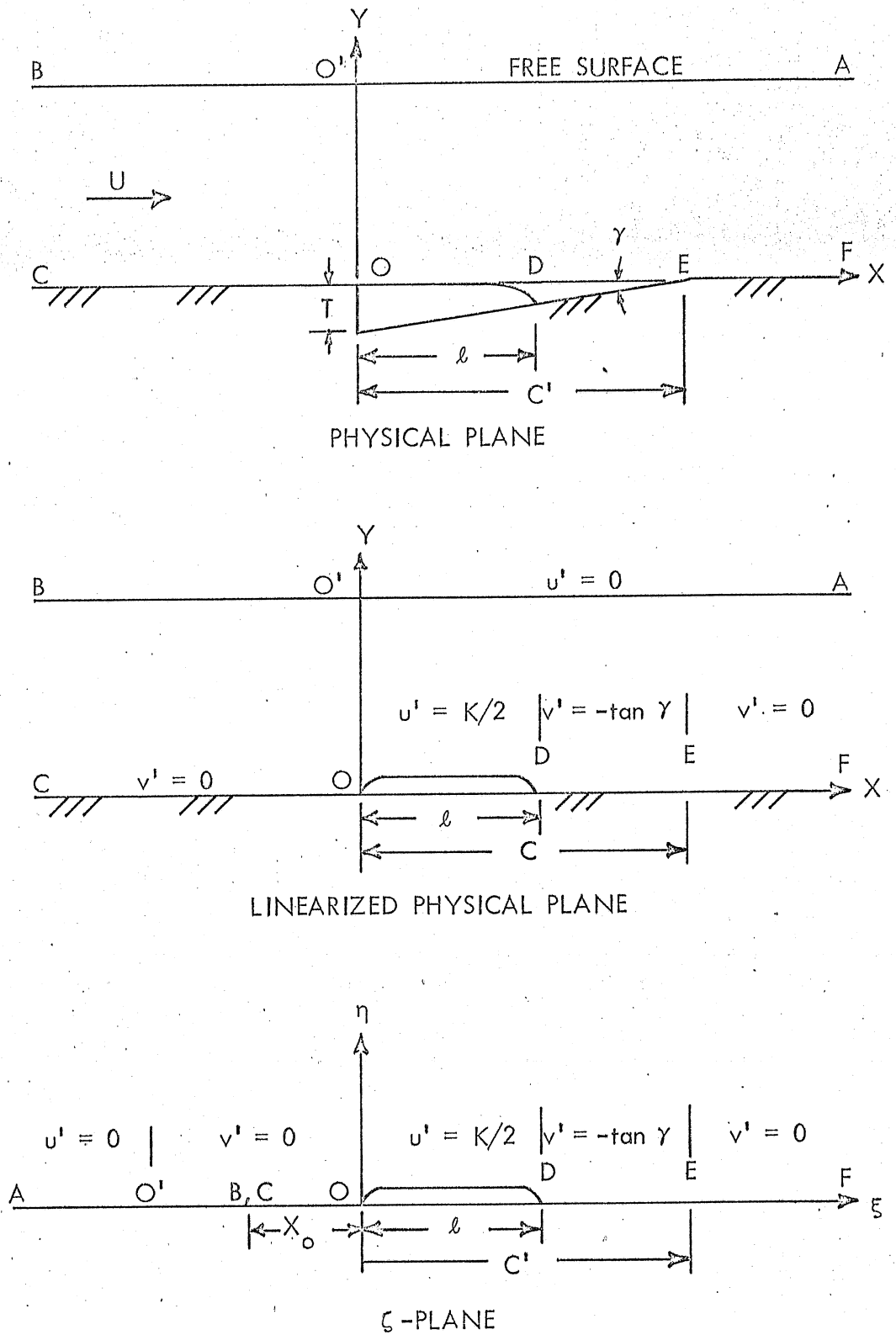


Fig. A-3 - Flow Configuration near the Slot